



Sizing of snow grains using backscattered solar light

Journal:	<i>International Journal of Remote Sensing</i>
Manuscript ID:	Draft
Manuscript Type:	IJRS Research Paper
Date Submitted by the Author:	
Complete List of Authors:	Kokhanovsky, Alex; University of Bremen, Institute of Environmental Physics Rozanov, V Aoki, Teruo Odermatt, Dani Brockmann, Carsten Krüger, Olaf Bouvet, Marc Drush, Mathias Hori, Masahiro
Keywords:	ALBEDO, SNOW
Keywords (user defined):	



Sizing of snow grains using backscattered solar light*

A. A. Kokhanovsky¹, V. V. Rozanov¹, T. Aoki², D. Odermatt³,
B. Brockmann⁴, O. Krüger⁴, M. Bouvet⁵, M. Drusch⁵, M. Hori⁶

¹Institute of Environmental Physics, University of Bremen, Germany

²Meteorological Research Institute, Tsukuba, Japan

³University of Zurich, Switzerland

⁴Brockmann Consult, Geesthacht, Germany

⁵European Space Agency, Noordwijk, The Netherlands

⁶Japan Aerospace Exploration Agency, Tokyo, Japan

* This paper is dedicated to the 80th birthday of Prof. A. P. Ivanov (Minsk, Belarus)

Abstract

In this paper, we describe a technique to determine the snow grain size from optical observations. The method is based on the analysis of the snow reflectance in the near IR, in particular the MERIS band at 865nm common to many spaceborne optical sensors is used. Also the algorithm is applied to MODIS 1240nm band. The sensitivity study is performed and it is shown which bands are superior with respect to information content as far as the snow grain size remote sensing is of concern. It is found that bands located at 1020 and 1240 μm are the most suitable for the snow grain size remote sensing applications. The developed method is validated using MODIS observations over flat snow deposited on a lake ice in Hokkaido (Japan).

1
2
3
4
5 **1. Introduction**
6

7 Understanding global physical properties of snow and also trends in snow cover
8 and pollution is of a great importance for a number of disciplines including climate
9 studies, environmental physics and snow hydrology (Dozier, 1987; Massom et al.,
10 2001). In this paper we address a question of subsurface snow grain size monitoring
11 using optical measurements. It is known that the snow grain size determines the level
12 of light absorbance by snow and this parameter is needed to asses the heat balance in
13 snow, and also timing and magnitude of snowmelt.
14
15
16
17
18

19 The first question, which is of importance to answer in this respect is the
20 definition of the grain size. Crystals in snow have diverse shapes and do not resemble
21 simple spherical particles such as occur, for instance, in fogs and water clouds.
22 Therefore, various sizes of snow grains are measured and reported. They include, e.g.,
23 the maximal and minimal dimensions of crystals, widths of branches, etc. However,
24 as far as remote sensing is concerned, the detailed structure of snow grains can not be
25 accessed. Only the effective optical size of grains can be derived. How this size can
26 be defined? For this one can use notions of average volume V and average projection
27 area S of a crystal. These parameters exist for any grain and in principle they can be
28 measured. Therefore, we define the effective grain size(EGS) a_{ef} as the ratio of these
29 parameters:
30
31
32
33
34
35
36
37
38

39
40
$$a_{ef} = \kappa \frac{V}{S}. \tag{1}$$

41
42

43 The parameter $\kappa=0.75$ is introduced to have the value of a_{ef} be equal to the radius
44 of particles for the case of ensembles of monodispersed spheres. In the case of
45 spherical polydispersions, a_{ef} has a simple sense of the ratio of the third to the
46 second moment of the size distribution. As theoretical modeling shows
47 (Kokhanovsky and Zege, 2004), the absorption cross section C_{abs} of snow grains in
48 the region of weak absorption is proportional to the volume of grains independently
49 on their shapes. Therefore, it follows:
50
51
52
53
54
55

56
$$C_{abs} = A\alpha V, \tag{2}$$

57
58
59
60

where A is the constant, which depends on the actual shape of a grain and also on the real part of refractive index $m = n - i\chi$, $\alpha = 4\pi\chi/\lambda$ is the bulk ice absorption coefficient at the wavelength λ . The spectral variation of A can be neglected in the first approximation. This is due to the fact that the real part of the ice refractive index does not change considerably in the visible and near infrared regions of the electromagnetic spectrum. On the other hand, the extinction cross section C_{ext} is proportional to the geometrical cross section of particles S if $a_{ef} \gg \lambda$, which is always the case for snow grains. Namely, it follows (van de Hulst, 1957):

$$C_{ext} = 2S. \quad (3)$$

Therefore, one derives for the probability of photon absorption (PPA) $\beta = C_{abs}/C_{ext}$ using equations (2), (3):

$$\beta = \frac{A\alpha V}{2S}. \quad (4)$$

This is a very important equation. It shows that the PPA is directly proportional to the effective radius a_{ef} of a grain:

$$\beta = \frac{2}{3} A\alpha a_{ef}, \quad (5)$$

where we used Eq. (1). Eq. (5) holds for the polydispersions of grains having different sizes and shapes as well. Then S and V are just average values of corresponding parameters with respect to the distribution of sizes and shapes. Actually, the parameter S (but not V) is influenced by orientation of grains. So it must be averaged with respect to the orientation of grains as well. Sometimes, the following approximation is used (van de Hulst, 1957; Kokhanovsky and Zege, 2004):

$$\langle S \rangle = \Sigma / 4, \quad (6)$$

where Σ is the surface area of a grain and brackets mean average with respect to the random orientation of a grain. This formula is exact in the case of randomly oriented convex bodies such as spheres, ellipsoids, cylinders, etc.

The snow reflection function is governed mostly by the value of the PPA (Kokhanovsky et al., 2005). Therefore, there is a possibility to determine a_{ef} using optical measurements on ground, aircraft or from a satellite (Dozier et al., 2009).

What is important here is the fact that the retrieved effective radius has a clear physical sense, which is not the case, e.g., if measurements with a microscope are used. Then a lot of averaging procedures must be performed to derive the value of a_{ef} as determined in Eq. (1). To the knowledge of authors, this procedure actually has never been done. Also such a measurement is difficult to make because snow is a very delicate matter and crystals can be easily broken during the sampling procedure.

Fortunately, there is a way around this problem. The specific surface area (SSA) of snow σ can be measured directly. It is defined as (Domine et al., 2008)

$$\sigma = \frac{\bar{\Sigma}}{\rho_i \bar{V}}, \tag{7}$$

where $\rho_i = 0.9167 \text{ g/cm}^3$ (at 0°C) is the density of ice and $\bar{\Sigma}$, \bar{V} are corresponding parameters averaged with respect to the size/shape distributions of grains. SSA gives, therefore, the surface area per mass and it is inversely proportional to the effective grain size introduced above:

$$\sigma = \frac{3}{\rho_i a_{ef}}, \tag{8}$$

where we used the approximation (6). The indirect prove of this relation for snow samples is given by Matzl and Schneebeli (2006). An important issue here is that there are well established methods of the direct measurements of SSA, which can be used for the validation of the EGS defined by Eq. (1) as derived, e.g., from satellite measurements. In particular, the methane adsorption technique (Legagneux et al., 2002), microtomography (Schneebeli and Sokratov, 2004), near – infrared photography (Matzl and Schneebeli, 2006), and stereology (Matzl, 2006) can be used. This means that optical measurements of a_{ef} enable the determination of SSA as well.

The retrievals of snow grain size using optical measurements have been performed by several research groups (Bourdelles and Fily, 1993; Fily et al., 1997; Zege et al., 1998; Polonsky et al., 1999; Nolin and Dozier, 1993, 2000; Nolin and Liang, 2000; Painter et al., 1998, 2003; Stamnes et al., 2007; Hori et al., 2007; Zege

et al., 2008; Lyapustin et al., 2009). In all cases a_{ef} (or the effective diameter $d = 2a_{ef}$) was retrieved.

The aim of this paper is to present the fast semi-analytical snow grain size retrieval algorithm based on optical measurements. It is applied to the data from Medium Resolution Imaging Spectrometer (MERIS), which is one of the main instruments on board the European Space Agency (ESA)'s Envisat platform and also to radiances measured by The Moderate Resolution Imaging Spectroradiometer (MODIS) developed by NASA and currently operating from TERRA and AQUA satellite platforms.

MERIS is composed of five cameras disposed side by side, each equipped with a pushbroom spectrometer. These spectrometers use two-dimensional CCDs. One of the sides of the detector is oriented perpendicular to the trajectory of the satellite and simultaneously collects, through the front optics, observations for a line of points at the Earth's surface (or in the atmosphere). The spectrometers acquire data in a large number of spectral bands, but, for technical reasons, only 16 of them are actually transmitted to the ground segment (one of which is required for the low-level processing of the raw data). This instrument thus provides useful data in 15 spectral bands (412, 443, 490, 510, 560, 620, 665, 681.25, 708.75, 753.75, 760.625, 778.75, 865, 885, 900nm), which are actually programmable in position, width and gain. In practice, these technical characteristics are kept constant most of the time to allow a large number of systematic or operational missions. The intrinsic spatial resolution of the detectors provides for samples every 300 m near nadir at the Earth's surface, and the pushbroom design avoids or minimizes the distortions (e.g., bow tie effects) typical of scanning instruments. This is known as the 'Full Resolution (FR)' product. The more common 'Reduced Resolution (RR)' products are generated by aggregating the FR data to a nominal resolution of 1200 m. The total field of view of MERIS is 68.5 degrees around nadir (yielding a swath width of 1150 km), which is sufficient to collect data for the entire planet every 3 days (in equatorial regions). Polar regions are visited more frequently due to the convergence of orbits. The viewing zenith angle of MERIS changes in the range 0 - 40 degrees. So the surface bidirectional effects are minimized.

MODIS is a key instrument aboard the Terra (EOS AM) and Aqua (EOS PM) satellites. Terra's orbit around the Earth is timed so that it passes from north to south across the equator in the morning, while Aqua passes south to north over the equator in the afternoon. Terra MODIS and Aqua MODIS are viewing the entire Earth's surface every 1 to 2 days, acquiring data in 36 spectral bands, or groups of wavelengths (see <http://modis.gsfc.nasa.gov/about/design.php>). Two bands are imaged at a nominal resolution of 250 m at nadir, with five bands at 500 m, and the remaining 29 bands at 1 km. A ± 55 -degree scanning pattern at the EOS orbit of 705 km achieves a 2330 km swath and provides global coverage every one to two days. The Scan Mirror Assembly uses a continuously rotating double-sided scan mirror to scan ± 55 -degrees and is driven by a motor encoder built to operate at 100 percent duty cycle throughout the 6-year instrument design life. The optical system consists of a two-mirror off-axis afocal telescope, which directs energy to four refractive objective assemblies; one for each of the VIS, NIR, SWIR/MWIR and LWIR spectral regions to cover a total spectral range of 0.4 to 14.4 μm .

The retrieval is based on the fact that the reflectance in the near infrared (e.g., at 865nm) depends on the probability of photon absorption in snow and, therefore, on a_{ef} , as it was discussed above. It shares many similarities with algorithms developed before (see, e.g., Zege et al., 1998, 2008; Stamnes et al., 2007; Tedesco and Kokhanovsky, 2007; Lyapustin et al., 2009). However, it also has some distinctive features mostly related to atmospheric correction, cloud screening and the look-up-table construction. The paper is structured as follows. In the next section we introduce the optical model of snow. Then we study the sensitivity of spectral reflectance to the EGS. The section four is aimed at the algorithm description and validation.

2. Optical model of snow

2.1. Theory

The most important part of any inverse problem solution is the formulation of the forward model. How do we present snow for the purposes of the modeling of light propagation and reflection? The direct way is to introduce a great number of ice grains of various shapes and sizes in contact and then run a Monte-Carlo method

specifying Fresnel reflection and transmission laws at the boundaries of grains and also absorption of photons inside of grains (Peltoniemi, 2007). However, this method is quite slow and can not be used for the fast inverse problem solution. Therefore, we pose the following question. Is it possible to use a simple model of a semi-infinite ice cloud for the snow reflectance modeling? Surprisingly, as comparisons with in situ measurements show, this is really the case (at least in the first approximation and especially for the dry snow). It follows that due to large sizes of particles and also due to their irregular shapes, close – packed effects do not have pronounce effects as far as snow reflectance is concerned (Kokhanovsky, 1998). This has been also confirmed using direct Monte – Carlo ray – tracing simulations of snow bidirectional reflection function (Peltoniemi, 2007; although some small changes like snow darkening for larger snow densities were found at some geometries and wavelengths). Due to this we can directly transfer well – known techniques developed in cloud remote sensing (Kokhanovsky, 2006) to the problem of grain sizing in snow. The first issue, which we confront here is the shape of grains. How do we specify it? Several possibilities can be followed in this respect. They are

- ❖ assumption of spherical grains;
- ❖ assumed size distribution for a given particle model;
- ❖ assumed size distribution for a linear superposition of different models of grains (say, plates and cylinders).

Actually, the retrieved grain size will depend on the assumption on the shape. This problem was not solved in cloud remote sensing as well and remains a largest source of uncertainty in the results of optical sizing for ice clouds in general. The assumption of spherical particles is not very realistic and must be discarded (Tanikawa et al., 2006; Xie et al., 2006). An important property of the model to be used is 1) to give asymmetry parameters close to measured in situ; 2) to give results similar to those reported in the ground measurements of snow angular reflectance; 3) to be as simple as possible. To meet all three criteria specified above, we used the model of fractal grains in our previous work (Kokhanovsky and Zege, 2004; Kokhanovsky et al., 2005). As it is known, the real-life example of fractals is ice crystals freezing on a glass window. The asymmetry parameter g for this model is equal to 0.76 in the visible, which is similar to values of g

reported from in situ measurements in ice clouds (Garrett et al., 2001). In particular, the mean value of g measured using airborne instrumentation for clouds saturated with respect to ice was 0.74 ± 0.03 .

The fractal model of ice crystals was first introduced by Macke et al. (1996) and it is quite simple conceptually. It is based on the second generation of Koch fractals. The model is built as follows:

- ❖ the initial tetrahedron is taken (the 0-th generation fractal);
- ❖ the smaller tetrahedrons are added to each plane of the particle (the first generation fractal, see Fig.10 given by Macke et al. (1996));
- ❖ the procedure is repeated at smaller triangles leading to particles of higher generations.

As a matter of fact we do not use in this work the deterministic fractal crystals described above. Instead, the randomized Koch fractals of the second generation are used. A distorted Koch-fractal is achieved by adding random displacements of the particle edges to the standard procedure of fractal generation. The degree of distortion is defined by the maximum displacement length divided by the lengths of the crystals segments. It was equal to 0.2 for the simulations used in this paper. Interestingly, that the phase function of randomized fractal grains is almost identical to the phase function of a stochastically deformed ice sphere with large deformation parameters (Macke et al., 1996; Muinonen, 1996). The only differences occur for scattering angles smaller than 30 degrees where the Koch-fractal provides some broad halos produced by the distorted tetrahedral structure. These halos are of no importance of the reflected light simulations. Therefore, we may state that irregularly shaped particles produce some robust light scattering pattern almost not sensitive to actual details of the crystal shape distribution. The randomized hexagonal crystals and fractal particles also have similar angular scattering patterns(see Fig.1). This is the reason behind of our approach, where we use just one shape to simulate the snow reflectance. Generally, the influence of particular shapes of particles on the reflectance could be quite dramatic, however. This is shown, in particular, by Xie et al. (2006).

We also do not use the polydispersion of fractal crystals and limit our investigation by the assumption that all crystals have the same size. This is due to the fact that the phase functions of large particles such as irregular snow grains do not depend on their actual dimension in the geometrical optics domain (Kokhanovsky, 2006) in the visible (outside of the forward peak). There is some dependence of the phase function on EGS in the near infrared due to absorption processes inside of crystals. However, corresponding effects can be neglected in the first approximation. Yet another supporting point is the fact that for retrievals we use the fractal crystal phase function to get the reflection function in the visible and we correct for absorption effects using notions of the asymmetry parameter g and the probability of photon absorption in the framework of asymptotic radiative transfer theory (Kokhanovsky and Zege, 2004).

It is assumed that the snow is very deep and therefore, the snow optical thickness does not enter our calculations. The PPA is determined as (Kokhanovsky and Nauss, 2005):

$$\beta = \beta_{\infty}(1 - \exp(-\alpha\ell)). \quad (9)$$

This formula was obtained fitting geometrical optics results derived with the Monte Carlo code described by Macke et al. (1996). The value of β_{∞} corresponds to the limiting case of an ice crystal, which absorbs all radiation penetrated inside the particle ($\alpha\ell \rightarrow \infty$). It can be calculated using the model of spherical particles because total reflection from an impenetrable sphere and a randomly oriented nonspherical convex particle coincides (van de Hulst, 1957). It follows that $\beta_{\infty}=0.47$ at $n=1.31$ (for ice). The particle absorption length (PAL) ℓ is proportional to a_{ef} (Kokhanovsky and Nauss, 2005):

$$\ell = Ka_{ef} \quad (10)$$

with the parameter K depending on the shape of particles. For weakly absorbing particles, it follows from Eqs. (9), (10):

$$\beta = \alpha\beta_{\infty}Ka_{ef} \quad (11)$$

and, therefore (see Eq. (5)),

$$K = \frac{2A}{3\beta_{\infty}}. \tag{12}$$

We found using geometrical optics Monte-Carlo simulations and fitting procedure implemented in ORIGIN that $K = 2.63$ for fractals.

This completes the description of the model as far as the local optical characteristics of snow are of concern (phase function, single scattering albedo $\omega_0 = 1 - \beta$ and their relationship to the size of particles).

The snow spectral and angular reflectance can be calculated solving the standard radiative transfer (RT) equation (Chandrasekhar, 1960) for specified values of ω_0 and the phase function. In principle, any RT code (Lenoble, 1985) can be used for this purpose. The software package SCIATRAN (Rozanov et al., 2005) was used in this work. In the next section we validate our model using ground measurements of snow reflectance under assumption of snow vertical and horizontal homogeneity.

2.2. Validation of the model

Because of complexity of the problem and many approximations used, it is of importance to validate the model introduced above using measurements. This will actually show how accurate we are in the selection of the phase function, for instance. To this end, we have used measurements of the snow reflection function performed on a lake ice (see Fig.2) in Hokkaido (Japan). For the complete validation of the model, the value of a_{ef} needs to be known. However, simultaneous measurements of this parameter and snow reflectance have not been performed. Therefore, only partial validation of the model is possible. In particular, we derive the albedo of single scattering from measurements itself (at the nadir observation and the relative azimuthal angle (RAA) of 90 degrees, see Table 1) and then we use this value of single scattering albedo in our radiative transfer simulations with SCIATRAN for the phase function of fractal grains shown in Fig.1. The results of such a comparison are shown in Fig.3. They confirm that the selected model is capable to describe the spectral and angular dependence of snow reflectance as measured in situ. Generally, the theoretical curves are within errors of measurements at viewing zenith angles

(VZA) smaller than 40 degrees. Generally, VZA is below 40 degrees for MERIS observations. The reflectance is more anisotropic in the near IR as compared to the visible. The value of the single scattering albedo at $0.55 \mu m$ was not retrieved because it is very close to one for pure snow located at the site. Therefore, we just plotted numerical results at $\omega_0 = 1$. This confirms that our model works both in the visible and near IR. Note that the performance of the model is worsen at oblique VZAs and RAA=0. The reflection function in the visible is essentially flat (close to the Lambertian surface assumption) at RAA=90°. This follows both from the theory and experiment.

Some deviations of the theory and experiment come from the experimental errors related to the shadowing of the sample by the instrument and also by the fact that the snow area under study was somewhat different for different viewing azimuthal angles.

The model is also capable to describe the hyperspectral snow reflectance. This was tested using the snow reflectance measurements in the Swiss Alps (Davos Dorf, see Fig.4) performed with a GER3700 instrument mounted on the Field Goniometer System (Sandmeier and Itten, 1999). The system depicted on Fig.4 is capable to measure the snow bidirectional reflectance function. The detailed description of the measurement system and the results derived is provided by Odermatt et al. (2005). The example of comparisons is shown in Fig.5, where we compare measurements and SCIATRAN calculations. It follows that SCIATRAN is capable to describe hyperspectral measurements as well. There is a discrepancy at $1.6 \mu m$, which do not appear in Fig.3. The cause of this discrepancy could be the variation of snow properties along the vertical not accounted for in the model. As a matter of fact, the value of a_{ef} varies with the height in snow and the use of the same radius at different wavelengths with a different penetration depth into snow (as it was done in Fig.5) is not justified (especially in the near IR, where the reflectance is sensitive just to the snow grains at the top). This problem does not exist for the results shown in Fig.3 because for each wavelength, the value of ω_0 (and not just single EGS for all

wavelengths as in Fig.5) was determined separately and this value most probably corresponds to different depths in a vertically inhomogeneous snow layer.

3. Sensitivity study

3.1. Theory

The radiance I over a snow field as detected on a satellite depends on the snow properties and also on atmospheric parameters in the propagation channel. The snow parameter of interest in this work is the snow grain size a_{ef} . The retrievals can be effected by the concentration of pollutants (CP) c . Therefore, it is of importance to derive both parameters simultaneously. So here we will study the sensitivity of the reflection function to the determination of both SGS and CP.

The derivatives of the reflectance $R = \pi I / \mu_0 E_0$ ($\mu_0 = \cos \vartheta_0$, ϑ_0 is the solar zenith angle (SZA), E_0 is the incident light irradiance) with respect to these parameters are defined as:

$$D_a = \frac{\partial R}{\partial a_{ef}}, D_c = \frac{\partial R}{\partial c}. \quad (13)$$

They help to understand if given measurements can be used to retrieve the pair (a_{ef}, c) . Clearly, derivatives depend on the viewing and illumination geometry (solar zenith angle ϑ_0 , viewing zenith angle ϑ , and the relative azimuthal angle φ), the spectral channel, values of (a_{ef}, c) , and also on the atmospheric conditions (primarily, through the aerosol optical thickness (AOT) τ). So, quite generally, we can write:

$$D = f(\vartheta_0, \vartheta, \varphi, \lambda, a_{ef}, c, \tau). \quad (14)$$

The task of this section is to understand how the derivatives D_a and D_c are influenced by various parameters given in Eq. (14). For this we use the software code SCIATRAN. In the framework of SCIATRAN derivatives are calculated through the following chain of equations.

First of all the weighting function (WF) W is introduced. We define it as (e.g., in the case of WF W_a for a_{ef} of a homogeneous snow layer):

$$W_a = \frac{\partial R}{\partial \ln a_{ef}} = a_{ef} D_a. \quad (15)$$

Clearly, this is a dimensionless quantity. Then, it follows, e.g., for the reflectance function at the effective radius a_{ef} :

$$R(a_{ef}) = R(\bar{a}_{ef}) + [a_{ef} - \bar{a}_{ef}] W_a / \bar{a}_{ef}, \quad (16)$$

if *a priori* assumed radius \bar{a}_{ef} is close to a_{ef} (so the linear approximation is valid).

Clearly, if $W_a = 0$, then the reflectance is not sensitive to a_{ef} . Similar equations can be written for WFs with respect to the concentration of impurities (W_c) and also AOT (W_τ). There are different ways to calculate weighting functions. One possibility is the numerical calculation of ratios $M = \Delta R / \Delta(\ln x)$, where x is equal to a_{ef} , c , or τ depending on the case considered. In SCIATRAN yet another approach for the calculation of derivatives is followed. It is faster as compared to the calculation of ratios M and also more accurate.

In particular, it is assumed that the variation of the reflectance δR due to the variation of the effective radius profile $\delta a_{ef}(z)$ inside the snow layer of the thickness H can be presented in the following form:

$$\delta R(\lambda) = \int_0^1 w_a(\lambda, z) \delta a_{ef}(z) dz. \quad (17)$$

Here z is the vertical coordinate divided by the thickness of the layer H . It follows that the information on the function $w_a(\lambda, z)$ is of a great importance for understanding how changes in the profile $a_{ef}(z)$ influence the variation in reflectance. The WF W_a is related to $w(\lambda, z)$ via the following equation:

$$W_a(\lambda, z) = w_a(\lambda, z) a_{ef}(z). \quad (18)$$

Then it follows:

$$\delta R(\lambda) = \int_0^1 W_a(\lambda, z) [\delta a_{ef}(z) / a_{ef}(z)] dz \quad (19)$$

or

$$\delta R(\lambda) = \sum_{k=1}^{N_k} J_a(\lambda, z_k) \frac{a_{ef,k}(z) - \bar{a}_{ef,k}(z)}{\bar{a}_{ef,k}(z)}, \quad (20)$$

where the summation is performed for the number of layers N_k inside of snow layer specified in the input of SCIATRAN and

$$J_a(\lambda, z_k) = W_a(\lambda, z_k) \Delta z_k \quad (21)$$

are correspondent Jacobians related to the sub-layer of thickness Δz_k . For a homogeneous layer it follows:

$$\delta R(\lambda) = [\delta a_{ef} / a_{ef}] W_a(\lambda, z) \quad (22)$$

and we return to the same expression as written above:

$$R(a_{ef}) = R(\bar{a}_{ef}) + \Delta R = R(\bar{a}_{ef}) + [a_{ef} - \bar{a}_{ef}] W_a / \bar{a}_{ef}. \quad (23)$$

The WF $W_a(\lambda, z_k)$ contains information not only on the dependence of R on a_{ef} but also on the sensitivity of the reflectance to the changes in the radii of grains at different layers inside the snow.

The derivatives

$$W_a(\lambda) = \sum_{k=1}^{N_k} J_a(\lambda, z_k) \quad (24)$$

and also Jacobians $J_a(\lambda, z_k)$ are main parameters discussed in the next section. The corresponding derivatives and Jacobians with respect to the concentration of pollutants and AOT are also considered.

As it follows from Eq. (20), W_a in Eq. (24) gives the change in the reflectance (δR) if the change in the radius is equal to 100%. The technique to derive $w_a(\lambda, z)$ using the solution of direct and adjoint radiative transfer equations is described by Rozanov et al. (2007).

3. 2. Results

The results of numerical experiments on the sensitivity studies are shown in Figs. 6-14. Let us analyze them now. All results were obtained using SCIATRAN (www.iup.physik.uni-bremen.de/~sciatran) and assuming that snow can be modeled

as an ice cloud with the optical thickness 5000 at the ground level (with fractal phase function shown in Fig.1). It was assumed that snow impurities (soot) are present in the form of Rayleigh scatterers and they influence only absorption and not scattering processes in a snow layer. The single scattering albedo was modeled using Eq. (38) (see also Eqs. (9), (41)). The LOWTRAN aerosol maritime model implemented in SCIATRAN with $\tau(550nm) = 0.05$ was used. Also the molecular scattering (but not absorption) has been taken into account. SCIATRAN is able to simulate satellite signals with account for the gaseous absorption. However, this was not needed for this work because only channels almost free of gaseous absorption have been selected.

We show the dependence of Jacobians $J_c(\lambda, z)$ for soot concentration on the distance from the snow bottom for several wavelengths in Fig.6. The top of snow layer is located at 1m height. It follows that Jacobians are different from zero only in the upper snow layers. They are about zero at depths 20cm (and larger) from the top in the visible. Therefore, the concentration of pollutants at very deep layers can not be retrieved from satellite observations. The maximum of the sensitivity is at some distance from the top of the layer and then the sensitivity decreases with the distance from the top. Most sensitivity comes from the upper 5cm of snow, if the visible channels are used. The sensitivity to soot concentration decreases with the wavelength and it happens more rapidly for larger snow grains (see, e.g., blue line on Fig.6). The main conclusion is that the shortest possible wavelength must be used for the soot concentration retrievals (e.g., at 400nm). Then the dependence of retrievals on the grain size can be largely ignored (see Fig.6).

Fig.7 is similar to Fig.6 but now the Jacobians for the effective radius of snow grains are given. The green curves correspond to the measurements at 1240nm. The upper panel of the figure corresponds to the case of $a_{ef} = 50\mu m$. It follows that the use of 1240nm channel is preferable (at least for the considered geometry). The channel at 1020nm is the second choice (red line on the left plots). Unfortunately, these channels are not available for ENVISAT instruments. So one must use 865nm (black lines on the left plots) for MERIS. Channels 1.61 and 2.2 μm of Advanced

Along-Track Scanning Radiometer (AATSR) on board ENVISAT can be also used. The channel at $2.2\ \mu\text{m}$ has slightly better performance (especially for large particles) as compared to the channel at $1.61\ \mu\text{m}$. The radiance in the $865 - 1240\text{nm}$ range is sensitive just to the snow properties at a top (e.g., $0.5\text{-}1\text{cm}$ from the top depending on the wavelength and also the size of particles, see Fig.7, left panels). The radiance at 1610nm and 2190nm is sensitive to changes of the crystals sizes only at a very top of the layer. As a matter of fact, the correspondent penetration depth is smaller than the SGS at these wavelengths (see right panels in Fig.7). Therefore, retrievals in the spectral range $865 - 1240\text{nm}$ range are most preferable with somewhat larger penetration depths (but smaller sensitivity) at 865nm .

The dependence of the derivatives W_a , W_c , and W_τ on the wavelength is given in Fig.8. The value of W_a is given by Eq. (24). The derivatives with respect to the concentration of a pollutant c and the aerosol optical thickness τ are defined in a similar way as for the value of a_{ef} . It follows from the analysis of this figure that the sensitivity to the soot concentration in snow disappears for larger wavelengths. This generally the case for the aerosol optical thickness as well. The behavior of the derivative with respect to the grain size (at a fixed wavelength) is nonmonotonous. At $a_{ef} = 50\ \mu\text{m}$, the most sensitivity comes from the larger wavelengths. For the sizes of 300 and $750\ \mu\text{m}$, the most sensitivity comes from the wavelengths in the middle of the spectral interval studied (1.02 and $1.24\ \mu\text{m}$). Therefore, there is no such a simple linear relationship to the wavelength in the sensitivity as in the case of the soot concentration. This is due to the fact that the influence of the size of grains on the reflectivity is small both at small values of the absorption parameter $b = \alpha a_{ef}$ and also at large values of this parameter. Therefore, the optimum is located at some middle values of absorption, which occurs at 1240nm for most practical situations. This also follows from the asymptotic radiative transfer theory. As it is shown by Kokhanovsky and Zege(2004) (see also the next Section): $R \sim \exp(-\nu\sqrt{b})$ (ν is the parameter not depending on b) in the limit of weak light absorption by snow

($\beta \rightarrow 0$). This means that $W_a \sim \sqrt{b} \exp(-\nu\sqrt{b})$ and $W_a \rightarrow 0$ at large and small values of b as it was discussed above.

It follows that $W_r(\lambda) \ll W_a(\lambda)$ and, therefore, generally the information on AOT is of no importance for the grain size retrievals. This conclusion is valid only at AOT=0.05 usual for clear polar conditions (Tomasi et al., 2008). The case of larger aerosol load (Arctic haze, e.g.) will be considered later on. Also we find that $W_c(\lambda) > W_r(\lambda)$ at channels 400 and 443nm. Therefore, these channels can be used for the soot concentration determination. However, the influence of uncertainty in the value of AOT on the retrievals of soot concentration is much larger as compared to the case of a_{ef} retrievals. We conclude that without accurate retrievals of AOT, the retrievals of soot concentration in snow are not possible. The derivatives in Fig.8 give the change in reflectance due to 100% change of a_{ef} , c , τ , respectively. We conclude that the signal at AOT=0.05 is influenced in the similar way by the soot concentration in snow and the aerosol optical thickness. So the accurate retrievals of AOT are of paramount importance for the soot concentration determination. This is also confirmed by data shown in Fig.9, which is similar to Fig.8 except AOT=0.1 (upper figures), AOT=0.5 (middle curves), AOT=1.0 (lower figures) are used in calculations. In all these cases (see figures on the right side) $W_c < W_r$ and, therefore, retrievals of soot concentration (at least at the level studied, $c = 10^{-8}$) are hardly possible without accurate information on aerosol optical thickness, which is difficult to retrieve over snow. As a matter of fact, both soot and aerosol can lead to the decrease of the registered signal and there is no technique in place to make a separation these two equally important contributions.

In Figs.10, 11, 12 the dependence of derivatives on the viewing zenith angle, the solar zenith angle, and the relative azimuth, respectively, is presented. The main conclusion is that the viewing geometry influences the grain size retrievals in smaller extent as compared to the retrievals of the soot concentration. Generally, retrievals of the soot concentration become more problematic at larger VZAs due to long paths of light in atmosphere. One can notice (see Fig.10) that the increase of VZA leads to the

increase in the sensitivity to the SGS at the wavelengths 1.6 and 2.1 μm . This is due to the fact that the snow brightness increases with VZA at these channels. Fig.11 shows the sensitivity of derivatives to the solar zenith angle. It follows that the sensitivity to the grain size increases for the high sun. However, in the regions, where there is permanent snow cover and generally, where snowfalls occur, the Sun is low and the sensitivity to the grain size (and also the soot concentration) decreases considerably. For the solar zenith angle 45° (and also for smaller SZA), there is a sensitivity of measurements to the soot concentration. However, such high solar zenith angles usually do not occur in the snow-covered regions. The sensitivity to the soot concentration drops significantly at SZA=75°. As it follows from Fig.12, the value of azimuth is also of importance as far as the sensitivity is of concern. The sensitivity is more pronounced at the relative azimuthal angle equal to zero degrees at the wavelengths 1.6 and 2.1 μm . For shorter wavelengths, the influence of the relative azimuthal angle RAA on the sensitivity of retrievals is quite low.

All results shown above correspond to the background level of soot concentration ($c = 10^{-8}$). Clearly, for larger soot concentrations, the sensitivity of reflectance to the soot concentration is larger (see Fig.13) and, therefore, c can be retrieved even if atmospheric correction is performed with considerable errors.

The most of findings reported in this section are summarized in Fig.14, which shows higher sensitivity to the soot content for larger values of c . Also one can see that generally, 1.02 and 1.24 μm channels are most suitable for the grain size monitoring from space.

4. Retrieval algorithm

4.1. Theory

The developed retrieval algorithm for the SGS determination is based on the look-up-table (LUT) approach. In particular, the Fourier components of the reflection function in the visible (for a nonabsorbing snow) are tabulated using the code developed by Mishchenko et al. (1999). The code solves the Ambartsumian nonlinear integral equation for the harmonics $R^m(\mu, \mu_0)$ of the reflection function.

These harmonics are stored in LUTs. Then the reflection function at any relative azimuth angle is found as

$$R(\mu, \mu_0, \varphi) = R^0(\mu, \mu_0) + 2 \sum_{m=1}^{M_{\max}} R^m(\mu, \mu_0) \cos(m\varphi). \quad (25)$$

Here $\mu = \cos \theta$ and the value of M_{\max} is chosen from the condition that the next term does not contribute more than 0.01% in the sum (25). In principle one more dimension (for a given phase function) in this LUT is needed and this is the dimension of the single scattering albedo. Taking into account that MERIS measurements stops at the wavelength $1\mu\text{m}$ and ice is only weakly absorbing in the spectral range of MERIS ($0.4-1\mu\text{m}$), we use the asymptotic radiative transfer theory for calculations of snow reflectance at absorbing wavelengths. This also simplifies the retrieval algorithm reducing it to analytical equations. Therefore, no minimization procedure is required.

In particular, we use the following representation valid as $\omega_0 \rightarrow 1$ (Zege et al., 1991; Kokhanovsky, 2006):

$$R(\mu, \mu_0, \varphi) = R_0(\mu, \mu_0, \varphi) A^{f(\mu, \mu_0, \varphi)}, \quad (26)$$

where

$$A = \exp\left\{-4s/\sqrt{3}\right\}, \quad s = \sqrt{\frac{1-\omega_0}{1-g\omega_0}}, \quad f = \frac{u(\mu_0)u(\mu)}{R_0^{-1}(\mu, \mu_0, \varphi)}, \quad u(\mu) = \frac{3}{7}(1+2\mu). \quad (27)$$

Here R_0 is the reflection function of a semi-infinite snow layer under assumption that the single scattering albedo is equal to one. It is calculated using Eq. (25).

The only approximation as compared to the exact RT calculations involved is the use of the exponential term in Eq. (26) to characterize light absorption by snow. The accuracy of this approximation is studied in Figs. (15)-(18). It follows that errors are below 6% as compared to SCIATRAN calculations at the wavelengths $0.52-1.24\mu\text{m}$ and $\text{SZA}=54^\circ$ for all azimuthal angles. Namely these short wavelengths will be used here for the inverse problem solution. In the case of MERIS wavelengths 443 and 865nm, the errors are smaller than 2% at $\text{VZAs}<40$ degrees typical for MERIS observations. This is well inside the calibration error of MERIS. If high accuracy is of

not primary concern than an approximation for the function $R_0(\mu, \mu_0, \varphi)$ given in Appendix can be used. This speeds up retrievals and make it easier to perform various types of sensitivity studies.

MERIS does not have channels above $1 \mu m$ and, therefore, the approximation proposed here is very relevant to the interpretation of MERIS observations over snow fields. This is due to the fact that the snow albedo (and the accuracy of the approximation) increases for shorter wavelengths. The forward model itself and also errors of atmospheric correction introduce much larger errors as compared to differences between approximate and exact theories.

Eq. (27) can be used for the analytical determination of ω_0 and, therefore, a_{ef} from the snow reflection function measurements. As a matter of fact in case of small grains and the MERIS wavelengths, even simpler approximation can be used. This approximation is followed from Eq. (26) as $\omega_0 \rightarrow 1$:

$$R(\mu, \mu_0, \varphi) = R_0(\mu, \mu_0, \varphi) - \frac{4s}{\sqrt{3}} u(\mu) u(\mu_0). \quad (28)$$

Eq. (26) also enables the determination of the snow spectral albedo:

$$A(\lambda) = (R_{mes}(\lambda) / R_0)^{1/f} \quad (29)$$

from measurements of the spectral reflection function just at one observation geometry. It is assumed that the atmospheric correction has already been performed and the influence of atmosphere is removed from the value of $R_{mes}(\lambda)$. The determination of the snow albedo also means that the snow reflection function $R = \pi I / \mu_0 E_0$ and the snow bi-directional reflection function $BRDF = R / \pi$ are also determined simultaneously at any viewing geometry (see Eq. (21)). Also the spectral snow similarity parameter is determined (see Eq. (27)):

$$s(\lambda) = \frac{\sqrt{3}}{4} \ln \left[\frac{1}{A(\lambda)} \right]. \quad (30)$$

This parameter is of importance for understanding of radiative transfer in snow.

The technique given above enables the determination of spectral characteristics $A(\lambda), s(\lambda), BRDF(\lambda)$ without a priori assumptions on the size of grains up to the

wavelength $1.24 \mu m$. We also found that the particular nonspherical grain shape assumption is not crucial for the snow albedo retrieval. In fact different assumptions on the grain shape produce very similar values of the spectral albedo.

The single scattering albedo can be found from the expression for the similarity parameter only if the value of the asymmetry parameter is known. At least for dry snow, one can assume that the asymmetry parameter only weakly depends on the wavelength and one can assume that $g = 0.76$ as discussed above independently on the wavelength (in the spectral range considered) as for fractal grains. For the wet snow, the value of g increases and the retrieval results for the single scattering albedo (but not the snow surface albedo) will be biased. One derives using Eq. (27) for s :

$$\omega_0(\lambda) = \frac{1 - s^2(\lambda)}{1 - gs^2(\lambda)} . \quad (31)$$

An important point is that although ω_0 will be possibly biased due to the assumption on the value of the asymmetry parameter, the spectral behavior of ω_0 is not effected by this assumption because (for large snow grains) g is almost spectrally neutral parameter. Moreover, because $gs^2 \rightarrow 0$ in the spectral range studied, the influence of the incorrect assumption on the value of the asymmetry parameter does not influence results for ω_0 considerably. In many applications not ω_0 but rather the probability of photon absorption is needed. It follows for this parameter:

$$\beta(\lambda) = \frac{(1 - g)s^2(\lambda)}{1 - gs^2(\lambda)} \quad (32)$$

and the error in $\varepsilon = 1 - g$ influences results considerably. However again, the spectrum $\beta(\lambda)$ is not much effected by the assumption on the value of ε because it is almost a spectrally neutral parameter in the spectral range considered.

The shape of particles must be assumed for the retrieval of the grain effective size from the value of PPA given by Eq. (32) using results presented above (see Eqs. (9), 10)). The value of the single scattering albedo in the near infrared ($\lambda \geq 0.8 - 1.0 \mu m$) is almost independent on the snow pollution. Therefore, it is proposed to find PAL and also a_{ef} in the near infrared (e.g., $1.02 \mu m$ or at $0.865 \mu m$ (MERIS/AATSR)). Then

the retrieved value of the grain effective radius can be used to determine the fraction of the PPA related to the pollution (in the visible). Actually, if one chooses the wavelength of 443nm, then the imaginary part of the refractive index of ice is so small ($\sim 10^{-10}$) that the whole absorption can be attributed to impurities and not to snow grains.

At the wavelength $0.865 \mu m$, there is a chance (for a highly polluted snow only) that the signal is contaminated by the contribution of pollutants. This contamination effect can be easily accounted for slightly modifying the algorithm described above.

Namely, we use the fact that it is possible to write for channels 1($0.443 \mu m$) and 2($0.865 \mu m$) in the approximation under study:

$$R_1 = R_0 \exp(-\gamma \sqrt{\beta_1}), \quad (33)$$

$$R_2 = R_0 \exp(-\gamma \sqrt{\beta_2}), \quad (34)$$

where indices 1 and 2 signify the channel,

$$\gamma = \frac{4f}{\sqrt{3(1-g\omega_0)}}. \quad (35)$$

We will neglect the difference of ω_0 from 1.0 in the dominator of Eq. (35).

Here we assume that there is some light absorption by snow even in the visible (e.g., due to soot). The value of probability of photon absorption can be written as

$$\beta = \frac{N_i C_{abs,i} + N_s C_{abs,s}}{N_i C_{ext,i} + N_s C_{ext,s}}. \quad (36)$$

Here

$$N_s = \frac{c_s}{\bar{V}_s} \quad (37)$$

is the number concentration of soot particles, \bar{V}_s is their average volume, c_s is the volumetric concentration of soot (the fraction of volume filled by soot), $C_{abs,\alpha}$ is the average absorption cross section of soot particles, $C_{ext,s}$ is the average extinction cross section of soot particles. Parameters with the index “i” have the same meaning as described above except for ice.

We will neglect the contribution of soot to the general light extinction in snow.

Then it follows:

$$\beta = \beta_i + \beta_s, \quad (38)$$

where $\beta_i = \frac{C_{abs,i}}{C_{ext,i}}$ is given by Eq. (9) and

$$\beta_s = \frac{V_i c_s C_{abs,s}}{V_s c_i C_{ext,i}}. \quad (39)$$

The average extinction cross section of the ice grains $C_{ext,i}$ can be estimated as follows (see Eqs. (3), (6)):

$$C_{ext,i} = \frac{\bar{\Sigma}_i}{2}. \quad (40)$$

Here $\bar{\Sigma}_i$ is the average surface area of grains. Taking into account that $C_{ext,i} / \bar{V}_i = 1.5 a_{ef}^{-1}$ in this approximation and also assuming that $C_{abs,s} / \bar{V}_s = B \alpha_s$, which is true in the Rayleigh domain for small soot particles ($B = 0.84$ at the soot refractive index $n = 1.75$ (van de Hulst, 1957), $\alpha_s = 4\pi\chi_s / \lambda$, $\chi_s = 0.46$), we derive:

$$\beta_s = \frac{2}{3} B c \alpha_s a_{ef} \quad (41)$$

where

$$c = c_s / c_i \quad (42)$$

is the relative soot concentration.

The mass absorption coefficient of soot $\sigma_{abs} = C_{abs} / \rho_s \bar{V}_s$ is equal to $B \alpha_s / \rho_s$ in the considered approximation. Here ρ_s is the soot density. Assuming that $B = 0.84$, $\chi_s = 0.46$, $\lambda = 443 \text{ nm}$, $\rho_s = 1 \text{ g / cm}^3$, one derives: $\sigma_{abs} = 8.4 \text{ g / m}^2$, which is close to the modern estimates of this parameter ($7.5 \pm 1.2 \text{ m}^2 / \text{g}$ (Bond and Bergstrom, 2006; Flanner et al., 2007)).

Therefore, we can write:

$$R_l = R_0 \exp \left[-\gamma \sqrt{\frac{2}{3}} B \alpha_{s,l} c a_{ef} \right], \quad (43)$$

$$R_2 = R_0 \exp(-\gamma \sqrt{\beta_{i,2} + \frac{2}{3} B \alpha_{s,2} c a_{ef}}). \quad (44)$$

Here we neglected light absorption by ice at the first wavelength. These two equations can be used to find both the size of ice crystals and the concentration of pollutants. It follows from the first equation for $X = c a_{ef}$:

$$X = \frac{3}{2B\gamma^2 \alpha_{s,1}} \ln^2 r_1 \quad (45)$$

and, therefore,

$$\beta_2 = \frac{\ln^2 r_2}{\gamma^2} - \frac{2}{3} B X \alpha_{s,2}, \quad (46)$$

where X is determined from Eq. (45). Here we introduced the normalized reflectance:

$r_i \equiv R_i / R_0$. The EGS can be found from Eqs. (9),(10):

$$a_{ef} = K \alpha_{i,2}^{-1} \ln \left[\frac{\beta_\infty}{\beta_\infty - \beta_2} \right]. \quad (47)$$

Then the concentration of soot is determined as $c = X / a_{ef}$. In practice, one measures the concentration of soot as the fraction of soot mass in a given mass of snow $c_f = c_s \rho_s / c_i \rho_i$, where ρ_s is the density of soot and ρ_i is the density of ice. Therefore, for the transformation of the satellite – derived c to the ground measured values of c_f , one must use the multiplier $\eta = \rho_s / \rho_i$:

$$c_f = \eta c. \quad (48)$$

We will assume that $\eta \equiv 1$ in this study. It is known that $\rho_i = 0.917 \text{ g/cm}^3$. The density of soot depends on its structure. It varies in the range $1\text{--}2 \text{ g/cm}^3$. The assumption of $\eta \equiv 1$ is consistent with the lower limit of this variability.

For MODIS, the channel at $1.24 \mu\text{m}$ is available in addition to $0.865 \mu\text{m}$ channel. The Global Imager (GLI, JAXA, currently not in operation) had several channels relevant to snow remote sensing (e.g., located at 0.865 , 1.05 and $1.24 \mu\text{m}$). The applications of the asymptotic radiative transfer theory for these sensors are given by Zege et al. (1998, 2008), Polonsky et al. (1999), Tedesco and Kokhanovsky (2007), and Lyapustin et al. (2009).

Generally, the wavelength $1.24\mu m$ is the best for retrievals in the case of a homogeneous snow because then even heavy pollution does not influence the results of the grain size retrieval (therefore, one can put $X=0$ in the expression for β_2 and derive the following simplified equation: $\beta_2 = \gamma^{-2} \ln^2 r_2$, which can be used in conjunction with Eq. (47) for the retrievals of a_{ef}). For vertically inhomogeneous snow, this wavelength brings information only from the top of the layer and may be not consistent with grains at deeper layers seen by the 443nm wavelength used for the snow pollution retrieval. Even if measurements at 865nm are used, there is quite large mismatch in the volume of snow sensed using 443nm and 865nm wavelengths. As it follows from Figs. 6, 7, the Jacobians for the soot concentration (at 443nm) approach zero at the distance of 20cm from the top layer and the values of Jacobians for the EGS vanish already 2-5cm depending on the wavelength. Therefore, possible soot layer deposited at, say, 5cm from the snow top will influence the signal in the visible but not at 865nm. This makes application of dual-wavelength algorithm not possible in this case and one should use the single channel algorithm based on Eqs. (47), (46) at $X = 0$.

It follows in the case of multiple pollutants:

$$\beta = \frac{N_i C_{abs,i} + \sum_{\alpha=1}^M N_{\alpha} C_{abs,\alpha}}{N_i C_{ext,i} + \sum_{\alpha=1}^M N_{\alpha} C_{ext,\alpha}} \quad (49)$$

Here

$$N_{\alpha} = \frac{c_{\alpha}}{V_{\alpha}} \quad (50)$$

is the number concentration of α -pollutant particles, V_{α} is their average volume, c_{α} is the volumetric concentration of α -pollutant (the fraction of volume filled by this particular pollutant), $C_{abs,\alpha}$ is the absorption cross section of the α -pollutant, $C_{ext,\alpha}$ is the extinction cross section of the α -pollutant. If dust is present in large quantities, the second term in the dominator of equation for β can not be ignored and such parameters as the size of dust grains and also their concentration must be

determined along with the parameters for soot. The necessity for such retrievals occurs only at rare occasions (heavy dust pollution events) and we will not explore this opportunity in this work.

4.2.Synthetic retrievals

To understand the sensitivity of the reflected radiation to the probability of photon absorption and the effective grain radius, we have performed a number of numerical experiments. In particular, we have implemented the retrieval algorithm in the numerical code and studied the influence of possible errors of forward model on the retrieval of PPA and a_{ef} . In particular, we have assumed that the measured reflectance differs by $\varsigma=\pm5\%$ or $\pm10\%$ from the forward model due to inherent calibration errors, errors of the forward model, cloud screening, atmospheric correction, etc. The resulting retrievals at the solar zenith angle equal to 54 degrees and nadir observations are given in Fig.19a. It follows that the positive bias in the measured reflection function leads to underestimation of PPA (and, otherwise, for the negative bias). At $\varsigma=0$, the algorithm retrieves input parameters with errors below several fraction of percent (see green line in Fig.19a), which is the prove of the algorithm with the synthetic data. It follows from Figs.19b that the error of PPA retrieval increases considerably as $\beta\rightarrow 0(\alpha a_{ef}\rightarrow 0)$. In particular, errors smaller than 20% (at a reasonable estimate of $\varsigma\sim 5\%$) are possible only if $\beta\geq 0.01$ ($\omega_0\geq 0.99$). Therefore, it is of importance to use spectral interval, where PPA varies in the range 0.01–0.02. The upper limit is needed to ensure small errors of the assumed asymptotic theory.

It follows from Fig.20 that the use of the wavelengths 1020 and 1240 nm is superior for the usually occurring grain sizes (0.05-1mm). The value of ω_0 at $\lambda=865nm$ is always smaller than 0.01 producing a reduced sensitivity to the effective grain radius. This is confirmed by Figs.21a,b, where we see that the value of $\varsigma=\pm5\%$ makes retrievals at the wavelength 865nm possible with the accuracy better than 50% only at radii larger than 0.4mm. Otherwise, retrievals are characterized by

quite large errors. This is unfortunate situation because the wavelength of 865nm is the largest, which can be used for retrievals using MERIS. The wavelengths of 885 and 900 nm are contaminated by the uncertainty in water vapor vertical column and also they are not much different with respect to the sensitivity to the grain size retrievals as compared to the wavelength 865nm. At the wavelength 1020nm, the errors of retrievals are smaller than 20%, if $\zeta = \pm 5\%$ at $a_{ef} \geq 0.2mm$ (see Fig.22a). The errors reach maximum of 50% at $a_{ef} = 0.1mm$. The errors are still lower at 1240nm (see Fig.22b) but then the use of asymptotic theory is in question (at least for large sizes of grains).

The measurements at the wavelength 443nm, where absorption of light by ice grains is small, can be used to retrieve the soot concentration in snow as described above. To get the concentration of pollutants, one must determine grain size (at least for large grains). Errors in the determination of the grain size influence the retrieval of soot concentration. In particular, errors are large, if the concentration of pollutants is small. Then the retrieved values of β_s are not reliable. One can estimate β_s assuming that $c = 300ng/g$, which is quite high concentration of pollutants. Then $\beta = 0.0002$ at $a_{ef} = 0.1mm$ and 0.002 at $a_{ef} = 1mm$. Clearly, these values of PPA are so small that the reliable determination of β and also $c \leq 300ng/g$ is hardly possible. And the values of the concentration above 300ng/g are extremely rare (Hansen and Nazarenko, 2004; Flanner et al., 2007). Therefore, it is proposed to make retrievals of β (at 443nm) only if the change of reflectance at this wavelength is considerable as compared to the case of pure snow. We show the difference of the calculated reflection functions of snow at PPA=0.0002 and 0.002 in Figs. 23a,b at incident angles 54 and 75 degrees as compared to the pure snow case. It follows that indeed retrievals at such levels of pollution are hardly possible due to errors of forward model. The concentration of soot in Arctic is just 10-30ng/g (Flanner et al., 2007) and PPA is always smaller than 0.0002. Then the retrievals of soot concentration are doubtful. The comparison of retrievals with ground measurements also confirms this conclusion (Aoki et al., 2007).

Because the analytical dependence of the reflectance on relevant parameters is

provided in the framework of our approach, it is also easy to calculate corresponding errors analytically. To simplify calculations, we use Eq. (28). Then after differentiation and some algebraic calculations, it follows for the uncertainty in the value of $b = \alpha a_{ef}$:

$$\frac{db}{b} = K_{amp} \frac{dR}{R}, \tag{51}$$

where the error amplification coefficient is given by the following equation:

$$K_{amp} = -\frac{2(R_0 - p\sqrt{b})}{p\sqrt{b}} \tag{52}$$

and

$$p = \frac{8Au(\mu)u(\mu_0)}{3\sqrt{3(1-g)}}. \tag{53}$$

The second term in the nominator of Eq. (52) can be neglected because it takes small value in the approximation under study. It follows that $K_{amp} \rightarrow \infty$ as $b \rightarrow 0$, the finding which follows from the numerical experiment given above and also from the sensitivity study presented in Section 3. Because the function $u(\mu)$ increases with the cosine of the angle, we conclude that K_{amp} is somehow reduced for oblique observation and illumination conditions (at least for angular regions, where R_0 is constant or decreases, e.g., see cases with the RAA in the range 90-180 degrees in Fig.3). The error amplification coefficient is proportional to $\sqrt{1-g}$ and, therefore, it is smaller for more extended in the forward direction phase functions.

4.3. Application of the algorithm to MERIS data

4.3.1. Cloud screening

For the determination of clear sky snow pixels, we use the differential snow index determined as

$$\varsigma = \frac{R(865nm) - R(885nm)}{R(865nm) + R(885nm)} \tag{54}$$

and also some criteria for $\Re = R(865nm)$. As a matter of fact, for clouds, reflectance increases with the wavelength in the spectral range 865-885nm and ς is often takes negative values. For snow and ice, ς is positive. The following assumptions have been introduced for the selection of clear sky snow pixels:

- ❖ $\varsigma > 0.01$;
- ❖ \Re is in the range 0.75-1.0;
- ❖ $|\varepsilon| < 0.001$, $\varepsilon = 1 - \frac{\bar{\Re}_{local}}{\Re_{middle}}$, $\bar{\Re}_{local}$ is the average of \Re for the seven neighboring MERIS pixels, \Re_{middle} is the value of reflectance for the pixel located in the middle of the seven selected pixels;
- ❖ \Re at any point in the particular area Σ does not differ by more than $\pm 10\%$ from the reflectance averaged for the scene (in the averaging procedure only pixels which pass conditions given above are used). The size of the area Σ depends on the snow field under consideration. Clearly, this condition can be applied only to the case of homogeneous snow fields (Antarctica, Greenland).

In addition, if thermal infrared measurements are available (like for MODIS), the following additional conditions are used to identify clear pixels over snow (Ackerman et al., 2006; Kokhanovsky and Shreier, 2008):

- ❖ brightness temperature $BT(11\mu m) > 250K$;
- ❖ $R(3.7\mu m) \geq 0.05$;
- ❖ temporal variability of $R(3.7\mu m)$ is checked. Several orbits are analyzed to see if the reflectance at $3.7\mu m$ at a given location is changed with time. For clear snow pixels, it is assumed that this change is small.

The reflectance at $3.7\mu m$ is calculated as follows (Spagenberg et al., 2001):

$$R(3.7\mu m) = \frac{(B - B^+)e}{\mu_0 S(3.7\mu m) - B^+e}, \quad (55)$$

where B is the measured brightness temperature at $3.7 \mu m$, B^+ is the $3.7 \mu m$ BT derived by using a Planck distribution for the measurement at $11 \mu m$, $e = 0.964$ is the clear snow emittance at $3.7 \mu m$, S is the solar constant.

4.3.2. Atmospheric correction

As far as atmospheric correction over snow is concerned, we used the LUT of atmospheric reflectances calculated with SCIATRAN for a prescribed aerosol model. Anyway, the influence of atmosphere on grain size retrievals is small as it was proved in the sensitivity studies. Therefore, such an approach is well justified (at least for a clear atmosphere). In the case of polluted atmospheres, the atmospheric contribution must be assessed using measurements at the neighboring pixels containing open water or polynyas. We demonstrate the importance of atmospheric correction in Figs. 24, 25, where results of SCIATRAN calculations are given for the case of the surface albedo equal to 0.8 and overlying aerosol layer. It follows that atmosphere substantially changes the values of reflectance as compared to the case $A=0.8$ especially at large solar and viewing zenith angles and for shorter wavelengths. An interesting point to note is that the atmospheric contribution can increase or decrease the satellite signal over the snow field depending on the geometry and, therefore, relative contribution of the atmosphere to the signal.

The following simplified atmospheric correction algorithm is proposed. It is supposed that the correction for the gaseous absorption can be performed as:

$$R_{cor} = T_{gas} R_{MERIS} , \tag{56}$$

where T_{gas} is the gaseous transmittance calculated as

$$T_{gas} = \exp(-\nu M) , \tag{57}$$

M is the trace gas vertical column (O_3 , H_2O as obtained from MERIS file), $\nu = 1/\mu + 1/\mu_0$, R_{meris} is the MERIS reflectance. The obtained reflectances R_{cor} (except at 760 and 900nm channels) are corrected for Rayleigh and aerosol scattering using the pre-calculated LUTs. It is assumed that the aerosol optical thickness is equal to 0.05 (see, e.g., Tomasi et al., 2007) in the calculation of LUTs. The aerosol model is WMO coarse maritime aerosol model with no absorption assumed. The angle grid was one degree for

SZA(0(1)89), VZA(0(1)80), and relative azimuth angle (0(1)180). Therefore, the largest possible mismatch of MERIS data and those in LUTs is 0.5 degree. The error due to this mismatch is smaller than 0.01 in the snow albedo, which is acceptable due to other complications inherent to snow properties retrievals. This is illustrated in Fig.26, where we show the retrieved albedo (retrieved using the pre-calculated LUTs described above) under assumption that true snow albedo is equal to 0.8. The synthetic data were generated not for the same grid as in LUT but for the 0.5-degree shifted LUT (for angles, the same shift was assumed). The algorithm performance is very good till VZA equal to 55 degrees, which is of importance for AATSR measurements. The largest MERIS VZA is 42 degrees and then the performance is even better (see Fig.26). The true albedo is retrieved if no shift in the grid is applied and the same snow and atmosphere models are used in the solution of direct and inverse problems. The change of the aerosol model in the retrieval process (from maritime coarse to maritime fine) does not bring complications, if the aerosol optical thickness was assumed to be the same (0.05). It follows that errors of retrievals are negligible even in the case if the aerosol model is not correctly selected (the errors are less than 0.01 in the snow albedo) as far as MERIS observations are of concern (VZA<42 degrees).

For the atmospheric correction, it is assumed that MERIS reflectance can be presented as

$$R = R_b + \frac{TR_s}{1 - Ar} \quad (58)$$

Here R_b is the MERIS reflectance for a black underlying surface (stored in LUTs for molecular-aerosol atmosphere with the assumed aerosol optical thickness of 0.05 and coarse maritime aerosol model with no absorption), R_s is the snow reflectance, T is the atmospheric transmittance stored in LUTs, r is the spherical albedo stored in LUTs, $A = 0.8$ is the assumed snow albedo. The term Ar is quite small. Therefore, the assumption on A does not make large impact on the retrieved snow reflectance:

$$R_s = (R - R_b)(1 - Ar)/T \quad (59)$$

The algorithm described above is of importance only for MERIS channels below 800nm, where the soot concentration and snow albedo is retrieved. The atmospheric

correction is less important at 865nm and also at 1020 and 1240nm, where the snow grain size is retrieved.

4.3.3. The retrieval of snow grain size using satellite observations

4.3.3.1. MERIS

The browse image of the snow field under clear sky in Greenland is shown in Fig.27. The corresponding maps of reflectances at 443nm, and 865 nm, and also in the oxygen A-band (762nm) are given in Fig.28.

A lot of clouds are present in the region. The retrieved grain size is shown in Fig.29a (after atmospheric correction and cloud screening procedures have been applied). The average EGS is around 0.2mm for the whole scene and 0.15mm for the left part of the scene, Unfortunately, *in situ* data for EGS at this location during the satellite measurements are not available to us.

We show the results of the retrieved concentration of pollutants in Fig.30 (in ng/g). The concentrations are very low as one might expect for Arctic. The somewhat increased concentration of pollutants in the right part of the image could be actually the effect of semi-transparent ice cloud (see, e.g., Fig.28b). Anyway, as it follows from the sensitivity studies given above, the accurate determination of soot concentration from a satellite is difficult in Arctic due to the low concentration of pollutants there. Although, as it is seen from Fig.28b, the magnitude of *c* is determined in a correct way.

4.3.3.2. MODIS

The validation of the algorithm has been performed using MODIS top-of-atmosphere spectral reflectances collocated (temporally and spatially) with ground measurements of snow properties in Hokkaido (Japan). The characterization of the validation sites is presented in Table 2. The experimentally measured grain sizes are given in Table 3. The maps of reflectances are shown in Figs. 31a-c. The retrievals have been performed for the snow field in the center of the image (red colour in Fig.31a). The algorithm developed by us (called FORCE) can be used for arbitrary channels. The channels of 460/865nm and also single channel at 1240nm have been

used in the retrievals. The map of EGS retrieved using channel at 1240nm is shown in Fig. 31d. It follows that the EGS is around 0.1mm for the area studied.

The corresponding MODIS data (500m spatial resolution) are presented in Table 4. The results of the inter-comparison of snow grain size retrievals (using channels 460nm, 1240nm) and ground measurements are given in Fig.32. In the case of satellite measurements the EGS is defined as the ratio of the average volume of particles to their average surface area multiplied by 3. Therefore, EGS coincides with the radius of particles in the case of monodispersed spheres. The EGS measured on the ground is denoted by r and it is equal to the half of the snow dendrite width (or a narrower portion of a broken ice crystal (Aoki et al., 2007)). Clearly, r and a_{ef} are different quantities. However, it is expected that they correlate. Indeed such a correlation exists as illustrated in Fig.32(the correlation coefficient is equal to 0.57), if channels 460 and 865nm are used both for the grains at the surface and also in deeper snow layers. As expected, the correlation increases (to 0.71), if the channel at 1240nm is used instead of 865nm (see Fig.33). The results of retrievals by FORCE give similar results as those derived by using independent EGS retrieval algorithm developed at JAXA (see Fig.33(Stamnes et al., 2007)).

The reason for a quite low correlation is further explained in Fig.35, where we plot the MODIS reflectance at 1240nm as the function of the EGS measured on the ground. According to the theory, all points in Fig.35 must lay on one line ($R \approx R_0 - K\sqrt{a_{ef}}$, where R is the measured reflectance, R_0 is the reflection function of nonabsorbing snow, and K is the coefficient of proportionality). As it follows from Fig.35, this is not the case. Generally, R decreases with the EGS, but this is just a general trend with many exceptions as shown in Fig.35. This points out to the difficulty of the correct grain size determination on the ground. One possibility to avoid this problem with ground measurements is to measure the EGS using light reflectance at the ground (say, at 1240nm) and not optical microscopy. Then the problems related to the manual determination of the grain size are not relevant anymore. Also it will make it possible to compare ground and satellite derived sizes

of crystals, which still may differ due to imperfect atmospheric correction and a poor sampling of satellite pixels by ground measurements.

5. Conclusions

In this work we proposed and validated a new snow grain size retrieval algorithm FORCE. The correlation coefficient between satellite and ground measurements of EGS is in the range 0.6-0.7. The reduced correlation coefficient could be due to the different definitions of sizes in the ground and satellite measurements. Also we proposed techniques for the cloud screening and atmospheric correction of satellite images over snow. The algorithm must be improved in future. The current version of the algorithm was implemented in the ESA software package BEAM and free for use by the remote sensing community.

Several simplifications have been used in the retrievals. In particular it was assumed that the snow is vertically homogeneous. In reality snow has a layered structure as discussed by Colbeck (1991). The layering arises from a sequence of storms, reworking of the snow surface into a distinctive horizon which is subsequent buried, or the generation of certain types of horizons within the snow profile. The sequence of these buried layers is not only unique from year to year and highly variable with location, but each layer also evolves as the snowy season progresses (Colbeck, 1982; 1983). Dust and soot can be deposited in such layers and then covered by the fresh snow. Because in standard retrieval algorithms vertically homogeneous snow is assumed, the pollutant content derived will be that of an entire snow column, which does not correspond to reality. Moreover, in retrievals one needs to assume the refractive index of the pollutants. The refractive index is considerably different for dust and soot. Also the absorption cross sections of soot and dust particles are considerably different. Therefore, wrong a priori assumptions on the type of pollutants (soot, dust, red algae on the surface of snow) prevent from correct retrievals of the concentration of pollutants. In principle, the type of pollutants can be distinguished from spectral measurements of the snow reflectance because, e.g., dust and soot have different spectral bulk absorption coefficients (e.g., red and grey

colours). However, this is possible only for thin covers of fresh snow over dirty snow or the freshly polluted snow cases.

Also as it follows that the structure of snow and also shapes/sizes of crystals are very different from the top to the bottom of the snow layer. This peculiarity is also not accounted in the forward model. The snow grain size is retrieved using infrared measurements. But it is a well known fact that the imaginary part of the refractive index of ice changes with the wavelength. This means that light with the different wavelengths will penetrate to the different depths. Therefore, the use of multiple wavelengths, in principle, can reveal the vertical distribution of the snow grains (Li et al., 2001; Zhou et al., 2003). Using one wavelength retrieval only one size for a given depth is retrieved. Importantly, the snow penetration depth is not fixed for a given wavelength but also it depends on the grain size itself. Generally, it is lower for larger wavelengths. Therefore, it is of importance to report at which wavelength the retrievals have been performed. If pollution is not uniformly distributed in snow but rather contained in distinct layers (e.g., dust), then one can not ignore light scattering by pollutants. Then both absorption and scattering effects by pollutants must be considered. Usually in retrievals of EGS, the pollution is assessed assuming the homogeneous distribution of snow layer. If pollution is in the layer well below the snow surface (see Fig.36), it plays no role in the EGS retrieval but it can play some role if pollutants are close to the surface and retrievals are done at the short wavelength (say 865nm) and grains are small.

Yet another problem is the possible existence of ice layer on the top of snow (crust). Crust snow is what happens when the surface of powder snow melts and then re-freezes. This action leaves a layer of ice on top of the snow that can make retrievals of the snow grain size underneath difficult, if this thin ice layer is not accounted for in the retrieval process properly. When the air temperature becomes warmer than the freezing point, the snow starts to melt and its water content becomes very high. With this, the delicate snow crystals change into large grains of ice and slush is formed. Slush is basically snow that is starting to melt and thus becomes further wet. Also satellite retrievals of snow grain size for very wet snow such as slush are not possible.

The radiative transfer models used extensively in the snow optics assume that snow has no structures on the surfaces. For satellite ground scenes (e.g., 1km²), the horizontal inhomogeneity of snow (e.g., sastrugi) may influence the snow BRDF and, therefore, the retrieved snow grain size considerably (Warren et al., 1998). We found that generally, the reflectances decreases, if sastrugi present and the decrease could be on the order of 5-30% depending on PPA. It is smaller for smaller PPA. The patches of vegetation penetrating through snow or trees make retrievals not possible or difficult. Therefore, it is of importance to make not only cloud screening but also only 100% snow covered ground scenes (without forest and vegetation) must be used in retrievals of the grain size, snow albedo, and the concentration of snow pollutants. This is due to the fact that there is a limitation with respect to the complexity of the forward model, which can be used in the retrieval process. Although there are some reports on the retrieval of subpixel snow properties (see, e.g., Painter et al., 1998, 2003, 2009). Retrieval of snow properties in the mountainous regions is also of problem. Then effects of shadowing are evident and 3-D radiative transfer models are needed with the known typography and illumination conditions at a given location.

The retrievals of grain size for polluted case (both for polluted snow and atmosphere) can cause problems, if the channel at 865nm is used for retrievals. This is due to the fact that the signal at 865nm can be influenced by pollution (Painter et al., 2007) and this influence is difficult to assess *a priori*. For instance, there is a problem of soot possibly present in atmosphere and in snow. For larger wavelengths, the influence of pollution is reduced considerably. Although Dozier et al. (2009) report that there are cases, where the pollution (e.g., dust) influences snow reflectance at all wavelengths in the visible and near infrared (up to $\lambda = 1.4 \mu m$). The retrieval of the pollution level depends on the type of pollution (Warren and Wiscombe, 1980; Warren, 1982; Painter and Dozier, 2004; Painter et al., 2007). The uncertainty in the imaginary part of the ice refractive index in the visible (Warren and Brandt, 2008) can also play a role.

As noted by Peltoniemi (2007), snow becomes less reflective at larger densities of particles. The radiative transfer theory can be applied at very low densities (actually not possible for snow on ground) only and, therefore, this darkening will be

interpreted as the presence of pollutants – although, in fact, the snow is fresh and clean. In particular, this could be the reason behind observed reduction of fresh snow reflectance in the visible as compared to radiative transfer simulations (see, e.g., Fig.5 provided by Dozier et al., 2009).

The radiative transfer model described above is valid for the dry snow only. During the melting season, water can accumulate in snow. Then the model must be changed taking into account the snow darkening due to the presence of liquid water in snow. Both modifications of snow absorption and scattering are important. The snow grains become more spherical and grow in size. Clusters are formed (Colbeck, 1979). The presence of liquid films between grains reduces the scattering and also it leads to more extended in the forward direction phase functions. This for sure will bias retrievals if not accounted for in the retrieval procedure. The issues highlighted above are a subject of our ongoing research on forward and inverse models in snow optics.

7. Acknowledgements

This work was supported by the ESA Project Snow_Radiance and also by JAXA (Japan). Alexander Kokhanovsky thanks Andreas Macke and Michael Mishchenko for providing their codes used in this study. We thank ESA and NASA for providing satellite data.

Appendix. Simple approximation for the reflection function

The reflection function $R_0(\mu, \mu_0, \varphi)$ can be calculated in the following approximation:

$$R_0(\mu, \mu_0, \varphi) = \frac{A + B(\mu + \mu_0) + C\mu\mu_0 + p(\theta)}{4(\mu + \mu_0)},$$

where $A=1.247$, $B=1.186$, $C=5.157$, $p(\theta)=11.1\exp(-0.087\theta)+1.1\exp(-0.014\theta)$, θ is given in degrees and defined as $\theta = a \cos(-\mu\mu_0 + ss_0 \cos \varphi)$, φ is the relative azimuth, $\mu = \cos(VZA)$, $\mu_0 = \cos(SZA)$. The accuracy of this approximation is better than 15% for the MERIS observation conditions (Kokhanovsky, 2006).

References

Ackerman, S., Strabala, K., Menzel, P., Frey, R., Moeller, C., Gumley, L., Baum, B., Wetzel, S., Seemann, S. and Zhang, H., 2006 : Discriminating clear sky from cloud with MODIS algorithm theoretical basis document (MOD35), at http://modis.gsfc.nasa.gov/data/atbd/atbd_mod06.pdf.

Aoki, T., Hori, M., Motoyoshi, H., Tanikawa, T., Hachikubo, A., Sugiura, K., Yasunari,T.J., Storvold,R., Eide, H.A., Stamnes, K., Li, W., Nieke, J., Nakajima,Y., Takahashi, F., ADEOS-II/GLI snow/ice products — Part II, 2007: Validation results using GLI and MODIS data. Remote Sensing of Environment, 111, 274-290.

Bond, T.C., and Bergstrom, R.W., 2006: Light absorption by carbonaceous particles: an investigative review, Aerosol Science and Technology, 40, 27-67.

Bourdelles, B., and Fily, M., 1993: Snow grain-size determination from Landsat imagery over Terre Adelie, Antarctica, Annals Glaciology, 17, 86–92.

Chandrasekhar, S., 1960: Radiative transfer, NY: Dover.

Colbeck, S.C., 1979: Grain cluster in wet snow, Journal of Colloid and Interface Sciences, 72, 371-384.

Colbeck, S.C., 1982: An overview of seasonal snow metamorphism, Review of Geophysics and Space Physics, 20, 45-61.

Colbeck, S.C., 1983: Theory of metamorphism of dry snow, Journal of Geophysical Research, 88, 5475-5482.

Colbeck, S.C., 1991: The layered character of snow covers, Reviews of Geophysics, 29, 81-96.

Domine F., Albert, M., Huthwelker,T., Jacobi, H.-W., Kokhanovsky, A., Lehning, M., Picard, G., Simpson, W. R., 2008: Snow physics as relevant to snow photochemistry, Atmospheric Chemistry and Physics, 8, 171-208.

Dozier, J., 1987: Recent Research in Snow Hydrology, Reviews of Geophysics, 25(2), 153–161.

Dozier, J., and Painter, T. H., 2004: Multispectral and hyperspectral remote sensing of alpine snow properties, Annual Review of Earth and Planetary Sciences 32, 465-494.

Dozier, J., Green, R.O., Nolin, A. W., Painter, T.H., 2009: Interpretation of snow properties from imaging spectrometry, Remote Sensing of Environment, 113, S25-S37.

Fily, M., Bourdelles, B., Dedieu J.P., and Sargent, C., 1997: Comparison of in situ and Landsat Thematic Mapper derived snow grain characteristics in the Alps, *Remote Sensing of Environment*, 59, 452–460.

Flanner, M. G., Zender, C. S., Randerson, J. T., Rasch, P. J., 2007: Present-day climate forcing and response from black carbon in snow, *Journal of Geophysical Research*, 112, D11202, .doi:10.1029/2006JD008003.

Garret, T. J., Hobbs, P.V., Gerber, H., 2001: Shortwave, single scattering properties of arctic ice clouds, *Journal of Geophysical Research*, 106, D14, 15,555-15,172.

Hansen J., Nazarenko L., 2004: Soot climate forcing via snow and ice albedos, *Proceedings of National Academy of Sciences of USA*, 101, 423-428.

Hori, M., Aoki, T., Stamnes, K., Li, W., 2007: ADEOS-II/GLI snow/ice products — Part III: Retrieved results, *Remote Sensing of Environment*, 111, 291-336.

Kokhanovsky, A. A., 1998: On light scattering in random media with large densely packed particles, *Journal of Geophysical Research*, 103(D6), 6089-6096.

Kokhanovsky, A. A., and Zege, E. P. , 2004: Scattering optics of snow, *Applied Optics*, 43, 1589-1602.

Kokhanovsky, A. A., Aoki, T., Hachikubo, A., Hori, M., Zege, E. P. , 2007: Reflective properties of natural snow: approximate asymptotic theory versus in situ measurements, *IEEE Transactions on Geosciences and Remote Sensing*, 43, 1529-1535.

Kokhanovsky, A. A., and Nauss, T., 2005: Satellite based retrieval of ice cloud properties using semianalytical algorithm, *Journal of Geophysical Research*, D110, D19206, doi: 10.1029/2004JD005744, 2005.

Kokhanovsky, A. A., Schreier, M., 2008: The determination of snow albedo using combined AATSR and MERIS observations, in *Proc. of the 2nd MERIS/(A)AATSR Workshop*, Frascati, Italy, 22-26 September 2008 (ESA SP-666, November 2008).

Legagneux, L., Cabanes, A., and Domine, F., 2002: Measurement of the specific surface area of 176 snow samples using methane adsorption at 77 K, *Journal of Geophysical Research*, 107 (D17), 4335, doi: 10.1029/2001JD001016.

Lenoble, J., 1985: *Radiative Transfer in Scattering and Absorbing Atmospheres: Standard Computational Procedures*, Deepak, Hampton.

Li, W., Stamnes, K., Chen, B., and Xiong, X., 2001: Snow grain size retrieved from near-infrared radiances at multiple wavelengths, *Geophysical Research Letters*, 28, 1699-1702, doi: 10.1029/2000GL011641.

Lyapustin, A., Tedesco, M., Wang, Y., Aoki, T., Hori, M., Kokhanovsky, A., 2009: Retrieval of snow grain size over Greenland from MODIS, *Remote Sensing of Environment*, 113, 1976-1987.

Matzl, M., 2006: Quantifying the stratigraphy of snow profiles, PhD Thesis, Swiss Federal Institute of Technology, Zürich.

Matzl, M., and Schneebeli, M., 2006: Measuring specific surface area of snow by near – infrared photography, *Journal of Glaciology*, 52, 558-564.

Mishchenko, M. I., Dlugach, J. M., Yanovitskij, E. G., Zakharova, N. T., 1999: Bidirectional reflectance of flat, optically thick particulate layers : an efficient radiative transfer solution and applications to snow and soil surfaces, *Journal of Quantitative Spectroscopy and Radiative Transfer*, 63, 409-432.

Muononen, K., Nusiainen, T., Fast, P., Lumme, K., and Peltoniemi, J. I., 1996: Light scattering by Gaussian random particles: ray optics approximation,” *Journal of Quantitative Spectroscopy and Radiative Transfer*, 55, 577–601.

Nolin, A. W., and Dozier, J., 2000: A hyperspectral method for remotely sensing the grain size of snow, *Remote Sensing of Environment*, 74, 207– 216.

Nolin, A. W., and Liang, S., 2000: Progress in bidirectional reflectance modeling and applications for surface particulate media: snow and soils, *Remote Sensing Reviews*, 18, 307-342.

Nolin, A.W. and Dozier, J., 1993: Estimating snow grain size using AVIRIS data, *Remote Sensing of Environment*, 44, 231–238.

Odermatt D., Schläpfer, D., Lehning, M., Schwikowski, M., Kneubühler, M., and Itten, I. K., 2005: Seasonal study of directional reflectance properties of snow, *EARSeL eProceedings*, 4, 203-214.

Painter, T.H., Roberts, D.A., Green, R.O., and Dozier, J., 1998: The effect of grain size on spectral mixture analysis of snow-covered area from AVIRIS data, *Remote Sensing of Environment*, 65, pp. 320-332.

Painter, T. H., Dozier, J., Roberts, D. A., Davis, R.E., and Greene, R.O., 2003: Retrieval of subpixel snow-covered area and grain size from imaging spectrometer data, *Remote Sensing of Environment*, 85, 64–77.

Painter, T.H., and Dozier, J., 2004: Measurements of the hemispherical – directional reflectance of snow at fine spectral and angular resolutions, *Journal of Geophysical Research*, 109, doi: 10.1029/2003JD004458.

Painter T. H., Barrett, A. P., Landry, C. C., Neff, J. C., Cassidy, M. P., Lawrence, C. R.,

McBride, K. E., Farmer, G. L., 2007: Impact of disturbed desert soils on duration of mountain snow cover, *Geophysical Research Letters*, 34, L12502, doi:10.1029/2007GL030284.

Painter, T. H., Rittger, K., McKenzie, C., Slaughter, P., Davis, R. E., and Dozier, J., 2009: Retrieval of subpixel snow covered area, grain size, and albedo from MODIS, *Remote Sensing of Environment*, 113, 868-879.

Polonsky, I.N., Zege, E.P., Kokhanovsky, A.A., Katsev, I.L., Prikhach, A.S., 1999: The retrieval of the effective radius of snow grains and control of snow pollution with GLI data, *Geoscience and Remote Sensing Symposium, IGARSS '99 Proceedings, IEEE 1999 International*, 2, 28 June-2 July 1999, pp. 1071 - 1073 vol.2, DOI: 10.1109/IGARSS.1999.774536.

Rozanov, V. V., Rozanov, A. V., Kokhanovsky, A. A., 2007: Derivatives of the radiation field and their application to the solution of inverse problems, in *Light Scattering Reviews*, v.2, p.205-265 (ed. by A. A. Kokhanovsky).

Rozanov, A. A., Rozanov, V.V., Buchwitz, M., Kokhanovsky, A. A., Burrows, J. P., 2005: SCIATRAN 2.0-a new radiative transfer model for geophysical applications in the 175-2400 nm spectral range, *Advances in Space Research*, 36, 1015-1019.

Sandmeier, S. R., and Itten, K. I., 1999: A field goniometer system (FIGOS) for acquisition of hyperspectral BRDF data, *IEEE Transactions on Geoscience and Remote Sensing*, 37, 978-986.

Schneebeli, M., and Sokratov, S. A., 2004: Tomography of temperature gradient metamorphism of snow and associated changes in heat conductivity, *Hydrological Processes*, 18, 3655-3665.

Stamnes, K., Li, W., Eide, H., Aoki, T., Hori, M., and Størø, R., 2007: ADEOS-II/GLI snow/ice products — Part I: Scientific basis, *Remote Sensing of Environment*, 111, 258-273.

Tanikawa, T., Aoki, T., Hori, M., Hachikubo, A., and Aniya, M., 2006: Snow bidirectional reflectance model using nonspherical snow particles and its validation with field measurements, *EARSel Proceedings*, 5 137-145.

Tedesco, M., and Kokhanovsky A. A., 2007: The semi-analytical snow retrieval algorithm and its application to MODIS data, *Remote Sensing of Environment*, 110, 317-331.

Tomasi, C., Vitale, V., Lupi, A., 2007: Aerosols in polar regions: A historical overview based on optical depth and in situ observations, *Journal of Geophysical Research*, 112, D16205, doi: 10.1029/2007JD008432.

van de Hulst, H. C., 1957: Light scattering by small particles, N. Y. : Wiley.

Warren, S.G., and Wiscombe, W.J., 1980: A model for the spectral albedo of snow. II: Snow containing atmospheric aerosols. *Journal of Atmospheric Sciences*, 37, 2734-2733.

Warren, S. G., 1982: Optical properties of snow, *Reviews of Geophysics*, 20, 67-89.

Warren, S. G., 1984: Optical constants of ice from the ultraviolet to the microwave. *Applied Optics*, 23, 1206- 1225.

Warren, S.G., Brandt, R.E., and Hinton, P., 1998: Effects of surface roughness on bidirectional reflectance of Antarctic snow, *Journal of Geophysical Research*, 103, 25789-25807.

Warren S. G., and Brandt, R.E., 2008: Optical constants of ice from the ultraviolet to the microwave: A revised compilation, *Journal of Geophysical Research*, 113, D14220, doi:10.1029/2007JD009744.

Xie, Y., Yang, P., Gao, B.-C., Kattawar, G. W., and Mishchenko, M. I., 2006: Effect of ice crystal shape and effective size on snow bidirectional reflectance, *Journal of Quantitative Spectroscopy and Radiative Transfer*, 100, 457-469.

Zege, E. P., Ivanov A. P., and Katsev, I. L., 1991: Image transfer through a scattering medium, Berlin: Springer.

Zege, E. P. , Kokhanovsky, A. A. , Katsev, I. L., Polonsky, I. N., and Prikhach, A. S., 1998: The retrieval of the effective radius of snow grains and control of snow pollution with GLI data, in *Proceedings of Conference on Light Scattering by Nonspherical Particles: Theory, Measurements, and Applications*, Mishchenko, M. I., Travis, L. D., and Hovenier, J. W., eds. American Meteorological Society, Boston, Mass., 288–290.

Zege, E. P., Katsev, I. L., Malinka, A., Prikhach, A. S., Polonsky, I. N., 2008: New algorithm to retrieve the effective snow grain size and pollution amount from satellite data, *Annals of Glaciology*, 139-144.

Zhou, X., Li, S., and Stamnes, K., 2003: Effects of vertical inhomogeneity on snow spectral albedo and its implications for remote sensing of snow, *Journal of Geophysical Research*, 108, 4738, 2003. doi: 10.1029/2003JD003859.

Tables

Table 1. The derived spectral single scattering albedo of snow and the corresponding measured reflection function at the nadir observation, SZA=54 ° and RAA=90 °.

$\lambda, \mu m$	ω_0	R(0°, 54°, 90°)
0.55	1.0	0.917
1.05	0.9958	0.692
1.24	0.9850	0.506
1.64	0.8650	0.141
2.21	0.8938	0.174

Table 2. The characterization of validation sites. * Measurements have been performed at several sites close to the indicated location (see Table 2 and Appendix 1). The range of the viewing zenith angles of MODIS and also solar zenith angle range is also given.

Site	Saroma *	Abashiri	Nakashibetsu
Latitude	44°07'09"N	43°58'15"N	43°29'56"N
Longitude	143°55'46"E	144°11'37"E	144°42'50"E
Underlying surface	Lagoon ice	Lake ice	Farmland
Date	05.02.2001 24.02.2002 26.02.2002	15.03.2004	22.03.2004 24.03.2004
SZA range, degrees	56.1-61.7	47.1-47.6	43.1-49.4
VZA range, degrees	1.5-22.5	12.9-20.8	0.1-54.9
Snow type	Dry	Wet	Wet, crust

Table 3. The grain size r measured on ground at various sites.

Case number	Date	Site	r , mm, deep layers	r , mm, upper layer
1	20010205	Saroma site C	0.309	0.095
2	20020224	Saroma site C	0.284	0.060
3	20020224	Saroma site 2	0.120	0.125
4	20020224	Saroma site 2'	0.169	0.75
5	20020224	Saroma site 6	0.280	0.125
6	20020224	Saroma site 5	0.194	0.150
7	20020224	Saroma site 7	0.366	0.163
8	20020224	Saroma site 8	0.335	0.150
9	20020224	Saroma site 3	0.438	0.188
10	20020224	Saroma site 4	0.114	0.100
11	20020226	Saroma site 8	0.296	0.275
12	20020226	Saroma site 5	0.218	0.073
13	20020226	Saroma site 4	0.111	0.105
14	20020226	Saroma site C	0.271	0.098
15	20020226	Saroma site 2	0.71	0.110
16	20040315	Abashiri	0.361	0.300
17	20040315	Abashiri	0.361	0.300
18	20040322	Nakashibetsu	0.411	0.375
19	20040322	Nakashibetsu	0.589	0.250
20	20040324	Nakashibetsu	0.432	0.500
21	20040324	Nakashibetsu	0.523	0.325

Table 4. MODIS satellite data for locations and time given in Table 3. The reflectance R shown in this table at a given wavelength (645, 865, 555, 1240, and 1640nm) is defined as $10000 \pi I / \mu_0 E_0$. Values of viewing zenith angle, viewing azimuth angle (VAZ), solar zenith angle, solar azimuth angle (SAZ), viewing azimuth angle (VAZ) also are given (in degrees, multiplied by 100). Each line in Table 4 coincides with a correspondent line in Table 3.

R645	R865	R460	R555	R1240	R1640	VZA	VAZ	SAZ	SAZ
7145	7780	7088	6791	4117	1097	145	10521	6167	16319
7933	8395	7974	7656	4911	1441	173	11059	5606	15873
7662	8093	7805	7484	4734	1344	176	11421	5607	15874
7646	8105	7747	7426	4824	1353	166	11417	5606	15875
7402	7679	7592	7269	4415	1281	182	11012	5606	15872
7390	7749	7512	7181	4440	1310	191	10970	5607	15870
7791	8208	7874	7557	4720	1338	165	11111	5605	15874
7763	8177	7859	7538	4809	1371	156	11169	5605	15876
7839	8319	8149	7843	5126	1572	166	10867	5605	15874
8100	8555	8135	7834	5239	1722	162	10485	5604	15873
7250	7689	7416	7018	3912	925	2215	9889	5618	15510
6754	7176	6979	6542	3625	878	2251	9885	5620	15504
7491	7889	7620	7214	4085	993	2234	10047	5618	15507
7154	7682	7362	6934	3942	925	2233	9887	5619	15507
7178	7688	7343	6943	3930	871	2233	9911	5620	15508
7038	6940	6778	6745	2741	766	2084	-7758	4763	16134
7203	6721	6877	6897	2144	506	1295	7854	4707	-16474
6837	6819	6329	6156	2755	767	3359	-7548	4392	16385
6994	6572	6806	6722	2242	461	12	1417	4446	-16035
6512	6226	6073	6107	1777	318	1532	-7872	4382	15949
6773	6234	6325	6400	1441	281	2102	7786	4306	-16421

Figure captions

Fig.1. The dependence of the phase function on the shape of particles. The following shapes were considered: hexagons with the length to the diameter ratios equal to 100/25, 100/50, 100/100 microns and fractal particles (Macke et al., 1996) at the wavelength 550nm. The diameter is defined as the distance between of opposite sides of the hexagon. For all particles the surface was assumed to be rough in the calculations. The asymmetry parameter g is given for each curve.

Fig.2. The measurement setup at Hokkaido (Japan). The measurements have been performed for snow deposited on flat lake ice.

Fig.3. The comparison of the measurements (crosses) and SCIATRAN (other symbols) calculations at several wavelengths. Measurements have been performed at Bihoro (Hokkaido, Japan, see Fig.2) at 11:30 local time on February 9th, 2001. The solar zenith angle is equal to 54 degrees and results for several relative azimuth angles (RAA) are given. The coordinates are 43°45'30.6"N, 144°10'28.8"E.

Fig.4. The measurement setup in Alps (Switzerland, 46.49N, 9.51E). The measurements have been performed for a deep snow layer in a valley on March 3, 2004 (11:59-12:47).

Fig.5. The comparison of spectral snow reflectance measured in Alps (Switzerland, 46.49N, 9.51E) at the solar zenith angle 53.9 degrees, relative azimuth angle of 45 degrees, and viewing zenith angle of 45 degrees. SCIATRAN calculations have been performed for an ice cloud model with the fractal ice grains (the length of the tetrahedron side $l = 290\mu\text{m}$). It was assumed that snow contains soot with the volumetric concentration $c = 10^{-7}$.

Fig.6. Dependence of the Jacobian for soot concentration $J_c(\lambda, z)$ on the distance from the snow bottom at the wavelengths 400, 443, 555, 670 nm (left, larger Jacobians at maximum correspond to a smaller wavelength) and at wavelengths 865 and 1029nm (right, larger Jacobians at maximum correspond to a smaller wavelength). The LOWTRAN aerosol model with the aerosol optical thickness (AOT) equal to 0.05 was used. The snow geometrical thickness is equal to 1m and the length of side of fractal particles is equal to 50 microns (upper panel), 300microns (middle panel), 750 microns (lower panel). The concentration of soot is equal to 10^{-8} . The solar zenith angle (SZA) is equal to 60 degrees and the observation is at the nadir direction.

Fig.7. Dependence of the Jacobian $J_a(\lambda, z)$ for effective radius of ice crystals in snow on the distance from the snow bottom at the wavelengths 865nm (black curve), 1020nm(red curve), and 1240 nm (green curve) (left panel). The same except at the wavelengths 1610nm(red) and 2190nm(black) (right panel). The LOWTRAN aerosol model with the aerosol optical thickness(AOT) equal to 0.05 was used. The snow geometrical thickness is equal to 1m and the length of side of fractal particles is equal to 50microns (upper panel), 300 microns (middle panel), 750 microns (lower panel). The concentration of soot is equal to 10^{-8} . The solar zenith angle (SZA) is equal to 60 degrees and the observation is at the nadir direction.

Fig.8. Dependence of the derivatives W_a for effective radius (left, red curve) and W_c for the soot concentration (right, red curve) on the wavelength (AOT(555nm)=0.05). Other parameters are the same as in Fig.7. Green lines give derivatives W_r for the aerosol optical thickness at 555nm.

Fig.9. The same as in Fig.8 except at AOT=0.1 (upper panel), 0.5(middle panel), 1.0(lower panel). The length side of fractal particles is 300 microns.

Fig.10. The same as in Fig.9 except at VZA=25 (upper panel) and 50 degrees (lower panel). The solar zenith angle is 60 degrees and the relative azimuth is 0 degrees.

Fig.11. The same as in Fig.10 except at SZA=45 (upper panel) and 75 degrees (lower panel).

Fig.12. The same as in Fig. 11 except at VZA=50degrees, SZA=60 degrees, azimuths 0 degrees(upper panel), 90degrees (middle panel) and 180 degrees(lower panel).

Fig.13. Dependence of the derivatives W_a for effective radius (left, red curve) and W_c for the soot concentration (right, red curve) on the wavelength. Other parameters are the same as in Fig.7. Green lines give derivatives W_r for the aerosol optical thickness at 555nm. The concentration of soot is equal to 10^{-8} (upper panel), 10^{-7} (middle panel), 10^{-6} (lower panel). The solar zenith angle (SZA) is equal to 60 degrees and the observation is at the nadir direction. The length of side of fractal particles is equal to 300microns .

Fig.14. Dependence of the derivatives W_a (left, 1-300 μm , 2-50 μm , 3-750 μm fractal particles) and W_c (right, 1-c= 10^{-8} , 2-c= 10^{-7} , 3-c= 10^{-6}) on the wavelength. The LOWTRAN aerosol model with the aerosol optical thickness (AOT) equal to 0.05 was used. The snow geometrical thickness is equal to 1m. The concentration of soot is equal to 10^{-8} for all curves on the left figure. The 300 μm fractal particles are used for all lines on the right figure (red colour). The green colour gives the derivative with respect to aerosol optical thickness. The solar zenith angle (SZA) is equal to 60 degrees and the observation is at the nadir direction (viewing zenith angle is equal to zero degrees).

Fig. 15. The dependence of the reflection function on the viewing zenith angle (lines - approximate theory with the use of LUTs for the reflection function of a non-absorbing semi-infinite snow, points – SCIATRAN calculations) for selected wavelengths and the SZA equal to 54 degrees. Lower lines for each wavelength correspond to the larger relative azimuthal angle equal to 0, 90 , and 180 degrees. The results are obtained using LUT for the function $R_0(\mu, \mu_0, \varphi)$ through the application of the nonlinear integral equation of Ambartsumian (Mishchenko et al., 1999).

Fig. 16. Error of the approximation shown in Fig.15. The upper curves correspond to the calculations at $1.24 \mu m$. Lower curves correspond to calculations at 0.52 and $1.05 \mu m$.

Fig. 17. The difference between reflectances at three azimuthal angles (0,90,180 degrees from top down) at wavelengths 443 and 865nm according to SCIATRAN (points) and MAA (lines). The SZA is equal to 54 degrees. SSA=1 at the wavelength 443nm . SSA=0.9994 at the wavelength 865nm. LUTs are used.

Fig. 18. Errors corresponding to the results shown in Fig. 17 at SSA=0.9994($\lambda = 865nm$).

Fig.19a. The retrieved PPA versus the assumed PPA at the incidence angle 54 degrees and the nadir observations.

Fig.19b The error of the retrieved PPA versus the assumed PPA at the incidence angle 54 degrees and the nadir observations.

Fig.20.The dependence of PPA on the effective grain radius.

Fig.21a. The retrieved effective grain radius versus the assumed grain radius at $\lambda = 865nm$ and SZA=54°.

Fig.21b The error of the retrieved EGS as the function of the assumed effective radius of grains retrieved at $\lambda = 865nm$.

Fig.22a. The error of retrieved EGS as the function of the assumed effective radius of grains at $\lambda = 1.02\mu m$.

Fig.22b. The error of the retrieved EGS as the function of the assumed effective radius of grains at $\lambda = 1.24\mu m$.

Fig.23a The difference of the reflection function from that for the case of a nonabsorbing snow as the function of the viewing zenith angle at azimuths 0, 90, 180 degrees, $SZA = 54^\circ$ ($SSA = 0.998$ and $SSA = 0.9998$).

Fig.23b The difference of the reflection function from that for the case of a nonabsorbing snow as the function of the viewing zenith angle at azimuths 0, 90, 180 degrees, $SZA = 75^\circ$ ($SSA = 0.998$ and $SSA = 0.9998$).

Fig.24a. The dependence of the reflectance $R(443nm)$ (upper panel) and $R(865nm)$ (lower panel) on the SZA and VZA at the relative azimuth angle equal to 0.0. The case of the underlying Lambertian surface with albedo 0.8 is presented for the maritime coarse aerosol model with aerosol optical thickness equal to 0.05. The values of reflectance are above 0.8 in the lower left corner and they well below 0.8 in the upper lower corner. This means that the Lambertian surface looks brighter from space, if observed from the nadir direction at $SZA = 0.0$. It looks darker for the nadir observation and the oblique solar light incidence (say, $SZA = 80$ degrees).

Fig.24b. The same as in Fig.24a except at $RAA = 90$ degrees.

Fig.24c. The same as in Fig.24a except at $RAA = 180$ degrees.

Fig.25. The dependence of the reflectance of the snow field with the assumed Lambertian albedo 0.8 on the SZA. The vertical lines give the variability due the variation of the viewing zenith angle (0(1)80degrees) and relative azimuth (0(1)180degrees). The atmosphere can increase or decrease the albedo of the snow field depending on the geometry. The aerosol optical thickness is 0.05 and the coarse maritime aerosol model is assumed.

Fig.26. The retrieved snow albedo as the function of the satellite and solar zenith angles. The aerosol optical thickness is equal to 0.05 and the fine mode maritime aerosol phase function was used in synthetic data preparation. The relative azimuth was varied in the range 0(1) 180 degrees. The true snow albedo is equal to 0.8. The upper panel differs from the lower panel due to the different regions of change of SZA and VZA. The range of SZA and VZA change is lower in the figure shown at the bottom.

Fig.27. Browse image of the scene analyzed. The retrievals have been performed for the clear sky portion of this image (upper left corner of the image).

Fig.28a. Maps of reflectances at 443nm (upper panel) and 865nm (lower panel) for the browse image shown in Fig.27. The cloud in the lower part of the image corresponds to the cloud in the write corner on Fig.27.

Fig.28b. The map of reflectance at 762nm (inside of oxygen absorption band).

Fig.29. The retrieved snow grain size (after cloud screening and atmospheric correction).

Fig.29b. The retrieved snow grain size histogram (the lower panel corresponds to retrievals in the left part of the image, where the influence of semi-transparent Ci clouds on the retrievals is less probable).

Fig.30. The retrieved concentration of pollutants.

Fig.31a. The map of MODIS reflectance at 460nm (multiplied by 10^4).

Fig.31b. The map of MODIS reflectance at 865nm (multiplied by 10^4).

Fig.31c. The map of MODIS reflectance at 1240nm (multiplied by 10^4).

Fig.31d. The retrieved grain size (the wavelengths 460 and 1240nm were used in retrievals).

Fig.32a. The correlation of satellite-derived and ground-measured grain size. The correlation coefficient is equal to 0.57.

Fig.32b The correlation of satellite-derived and ground-measured (at deeper layers) grain size. The correlation coefficient is equal to 0.57.

Fig.33. The correlation of satellite-derived and ground-measured grain size. The correlation coefficient is equal to 0.73 (and 0.81, if one single point (around 1.3mm) is removed).

Fig.34. The correlation of satellite-derived grain sizes. The correlation is very good except for two points.

Fig.35. The dependence of satellite reflectance at 1240nm on ground-measured grain size.

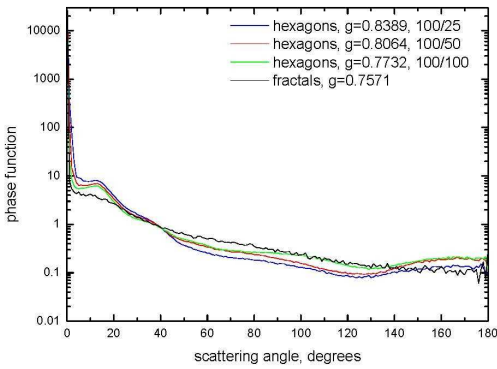


fig.1
215x279mm (200 x 200 DPI)



fig.2
215x279mm (223 x 222 DPI)

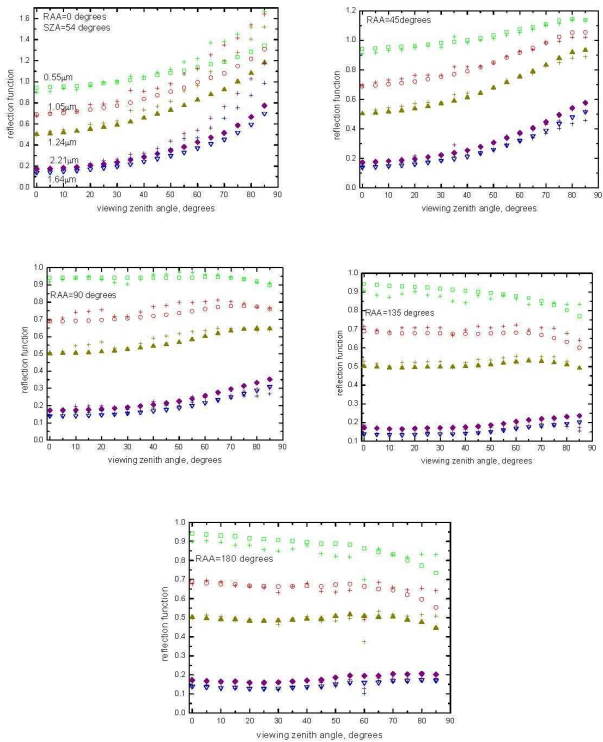


fig.3
215x279mm (200 x 200 DPI)



fig4
215x279mm (150 x 150 DPI)

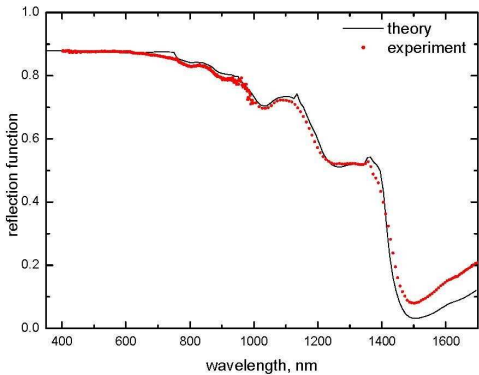


fig5
215x279mm (200 x 200 DPI)

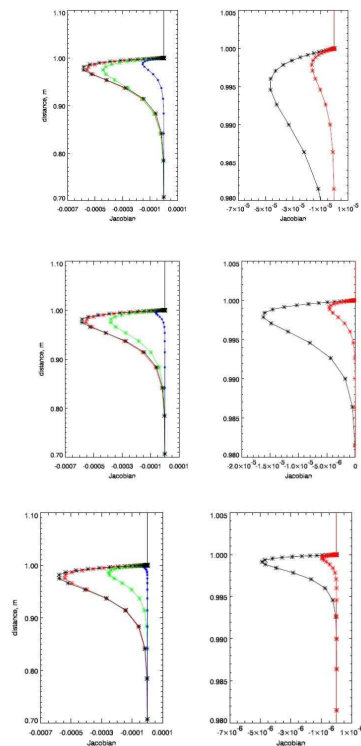


fig6
215x279mm (220 x 220 DPI)

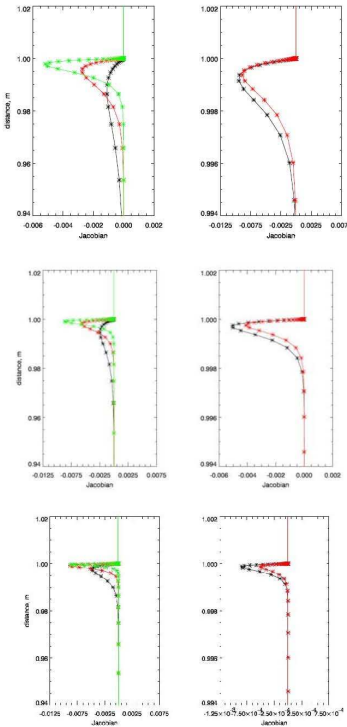


fig7
215x279mm (200 x 200 DPI)

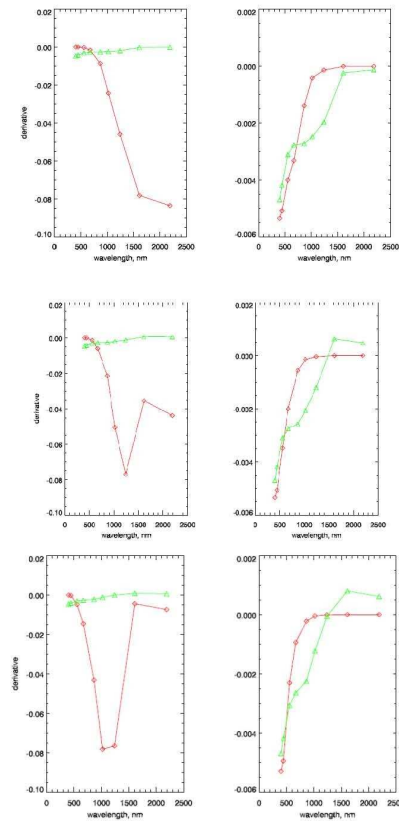


fig8
215x279mm (184 x 184 DPI)

1
2
3
4
5
6
7
8
9
10
11
12
13
14
15
16
17
18
19
20
21
22
23
24
25
26
27
28
29
30
31
32
33
34
35
36
37
38
39
40
41
42
43
44
45
46
47
48
49
50
51
52
53
54
55
56
57
58
59
60

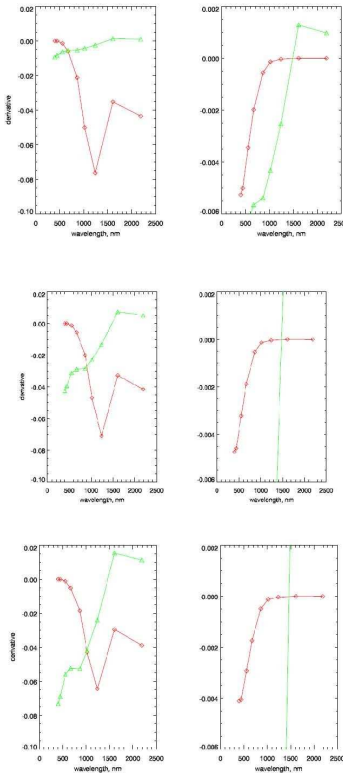


fig9
215x279mm (201 x 202 DPI)

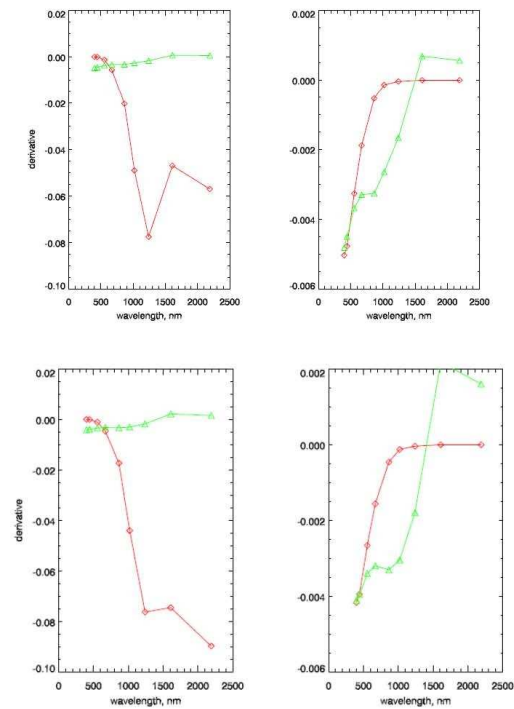


fig10
215x279mm (149 x 150 DPI)

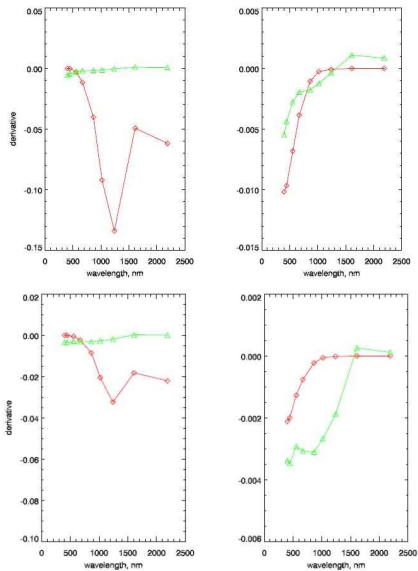


fig11
215x279mm (173 x 173 DPI)

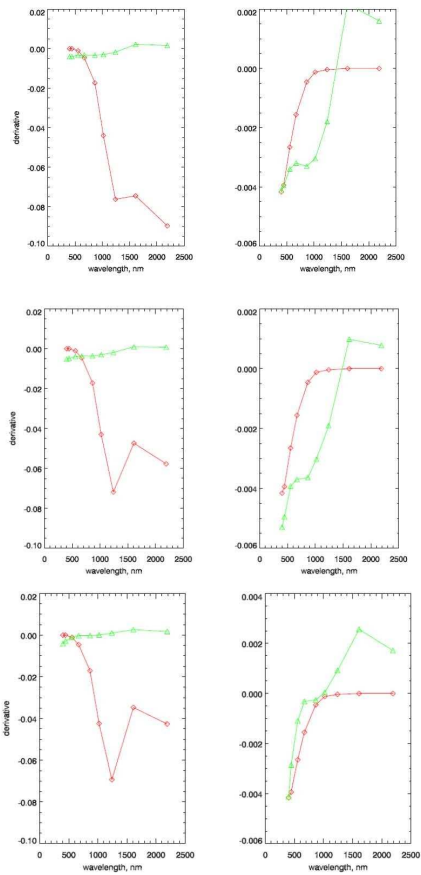


fig12
215x279mm (203 x 202 DPI)

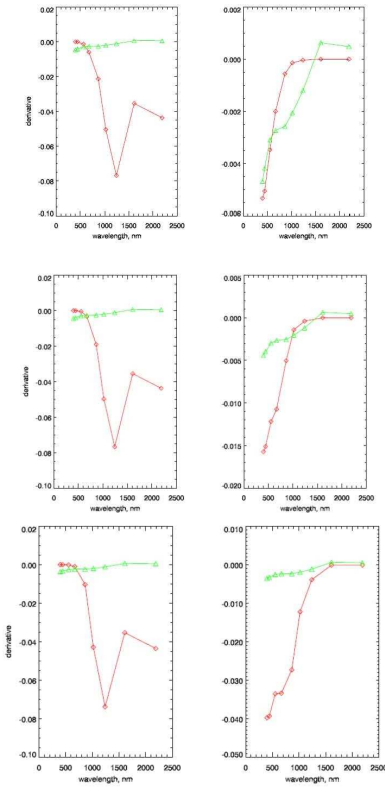


fig13
215x279mm (201 x 201 DPI)

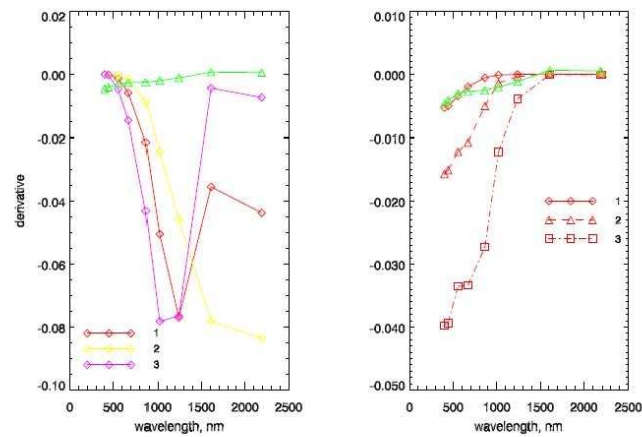


fig14
216x279mm (111 x 111 DPI)

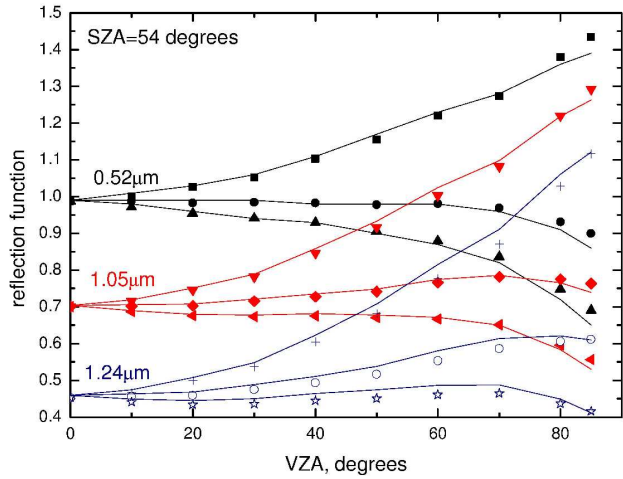


Fig.15
202x273mm (600 x 600 DPI)

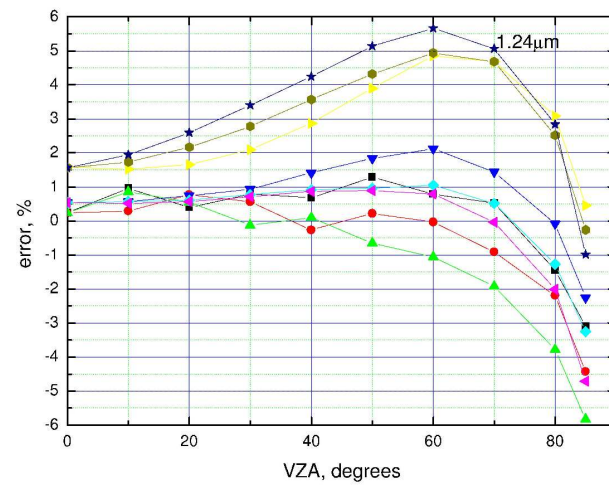


Fig.16
202x273mm (600 x 600 DPI)

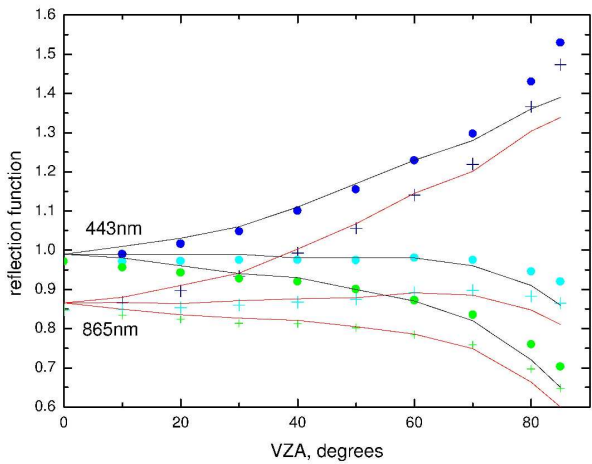


Fig.17
202x273mm (600 x 600 DPI)

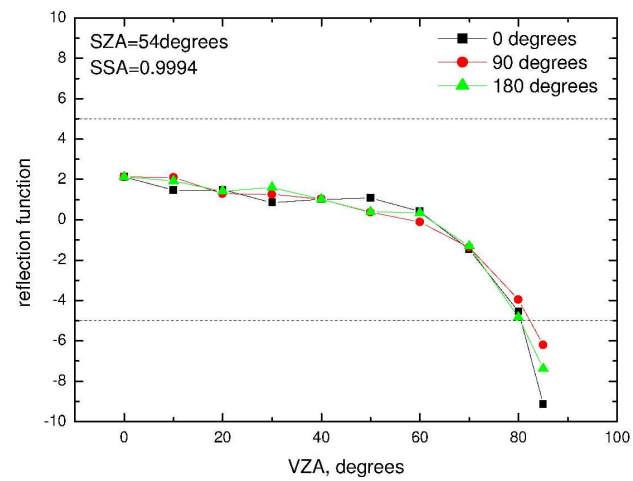


Fig.18
202x273mm (600 x 600 DPI)

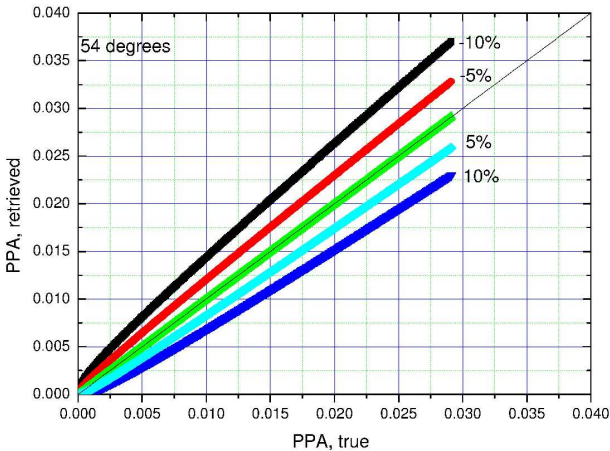


Fig.19a
202x273mm (600 x 600 DPI)

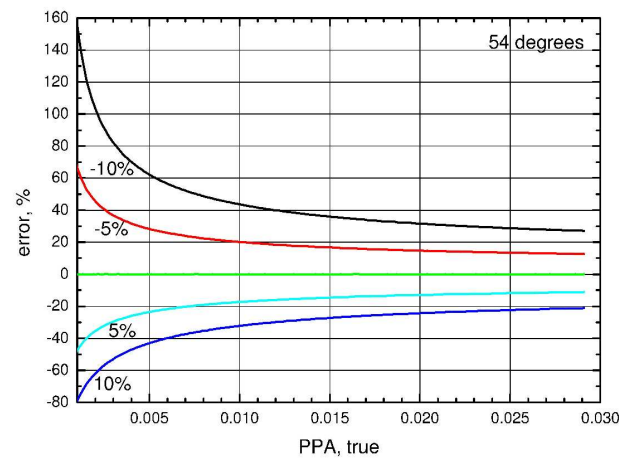


Fig.19b
202x273mm (600 x 600 DPI)

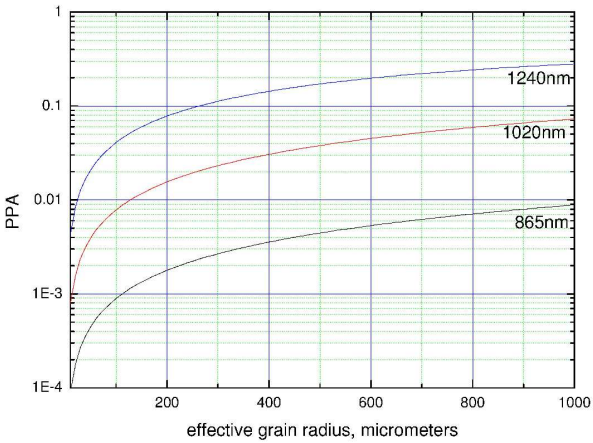


Fig.20
202x273mm (600 x 600 DPI)

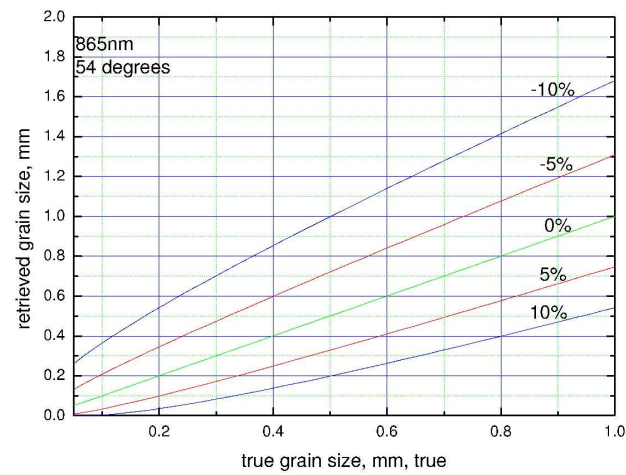


Fig.21a
202x273mm (600 x 600 DPI)

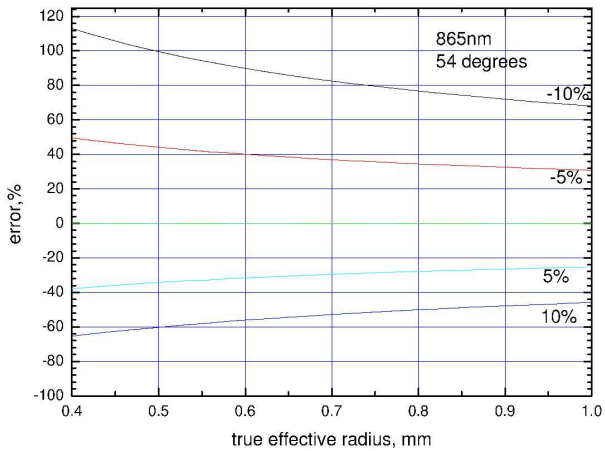


Fig.21b
202x273mm (600 x 600 DPI)

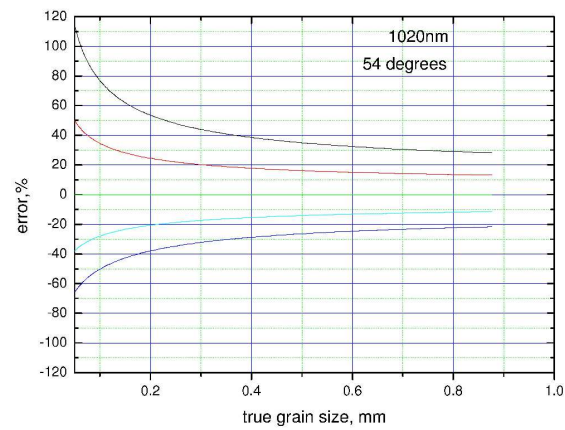


Fig.22a
202x273mm (600 x 600 DPI)

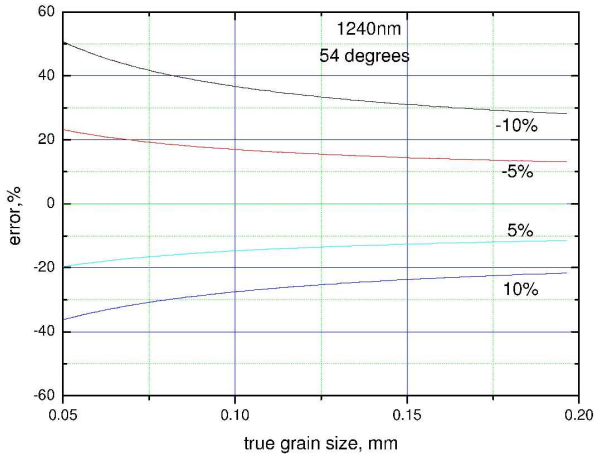


fig22b
202x273mm (600 x 600 DPI)

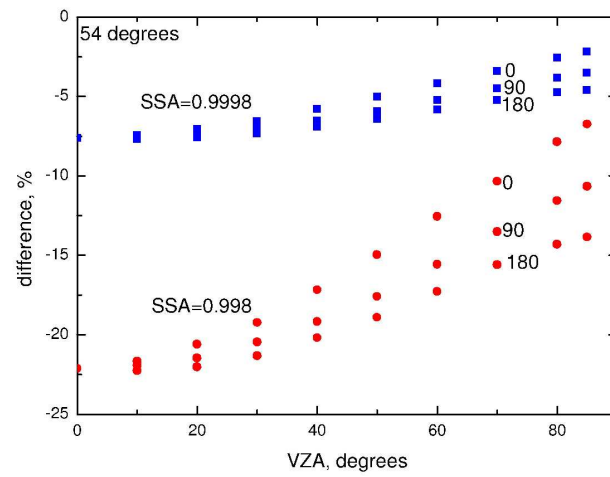


Fig.23a
202x273mm (600 x 600 DPI)

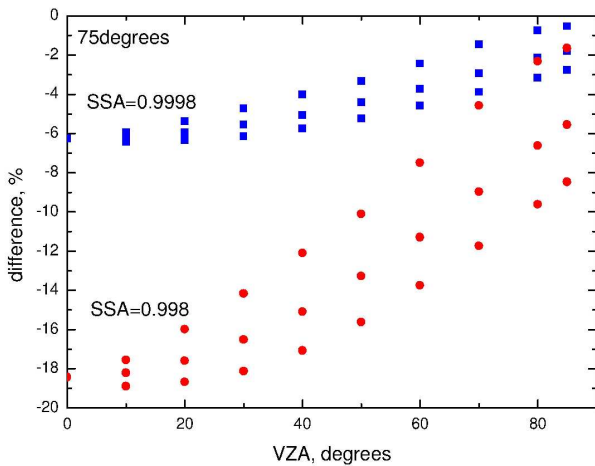


Fig.23b
202x273mm (600 x 600 DPI)

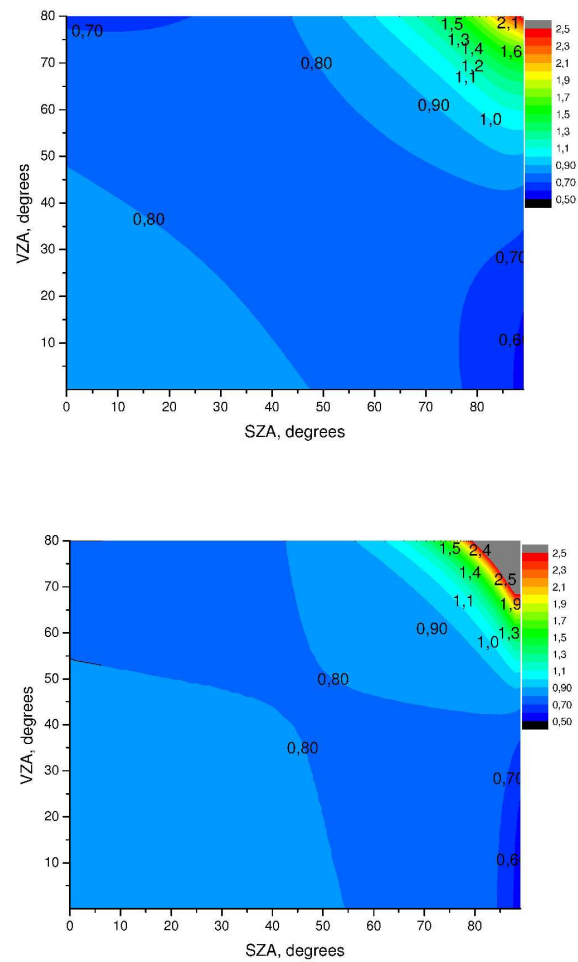


Fig.24a
202x273mm (600 x 600 DPI)

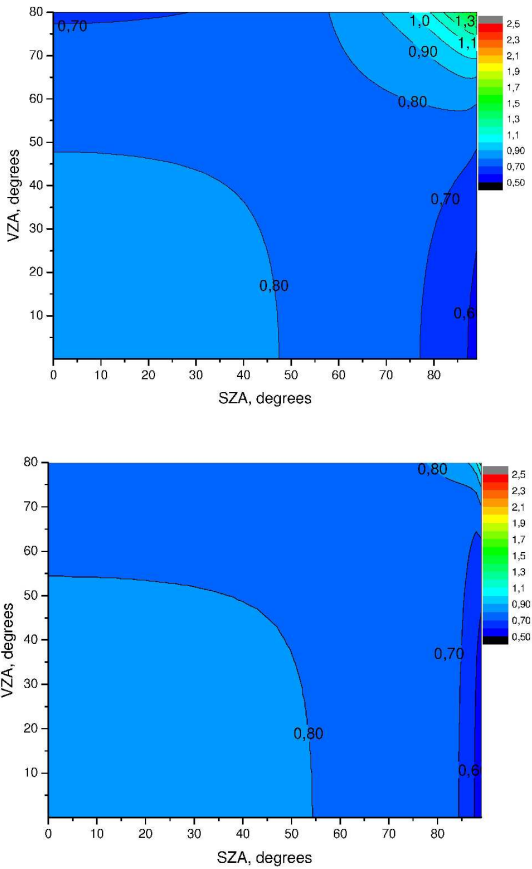


Fig.24b
202x273mm (600 x 600 DPI)

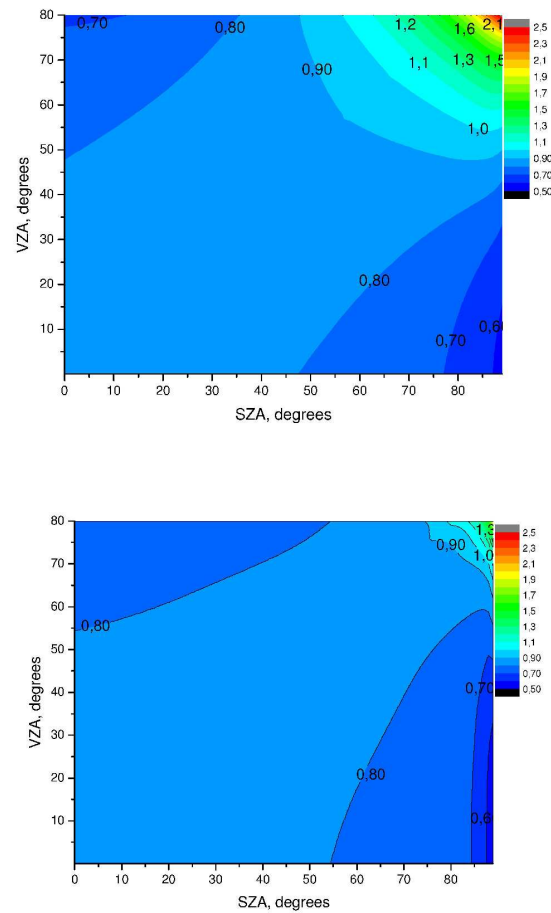


Fig. 24c
202x273mm (600 x 600 DPI)

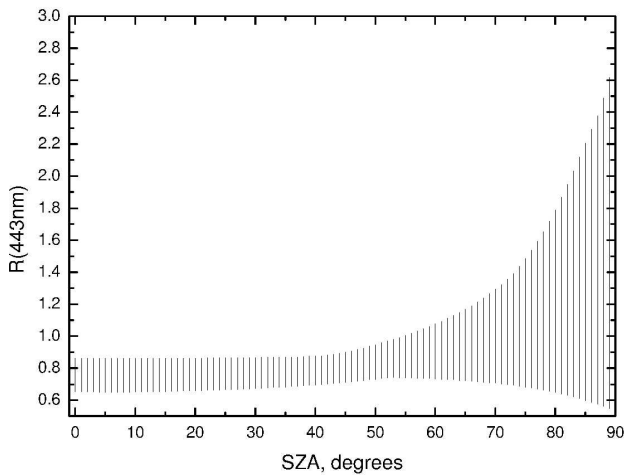


Fig.25
202x273mm (600 x 600 DPI)

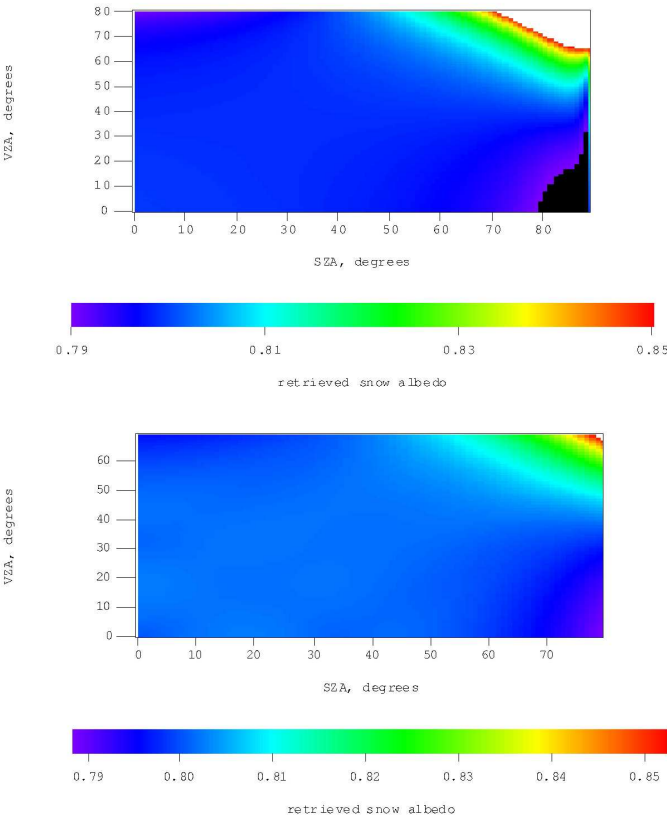


Fig.26
202x273mm (600 x 600 DPI)

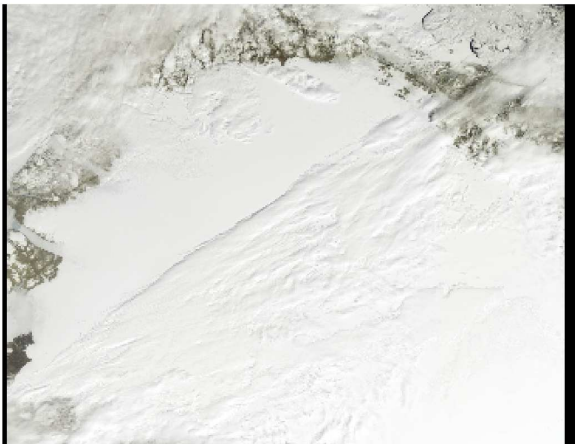


Fig.27
202x273mm (600 x 600 DPI)

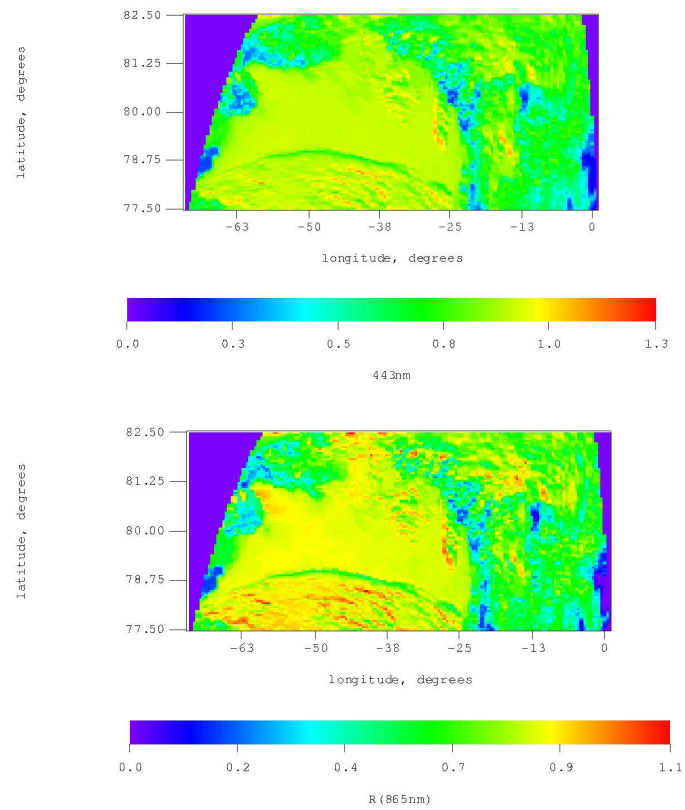


Fig.28a
202x273mm (600 x 600 DPI)

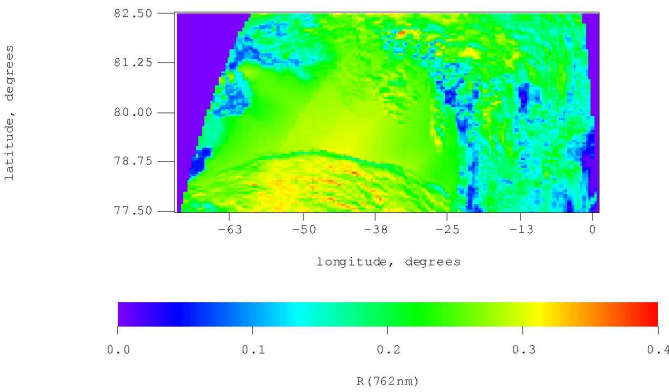


Fig.28b
202x273mm (600 x 600 DPI)

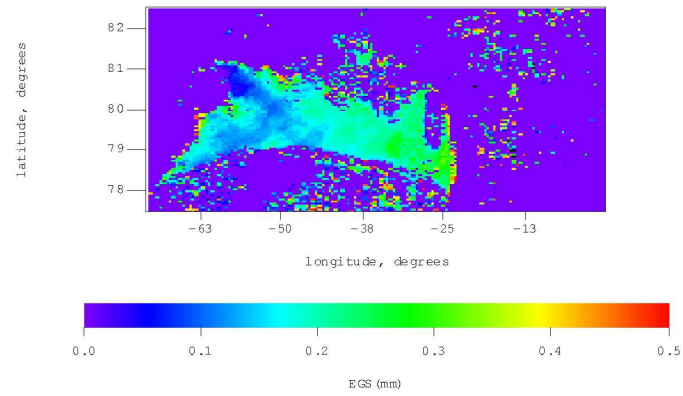


Fig.29a
202x273mm (600 x 600 DPI)

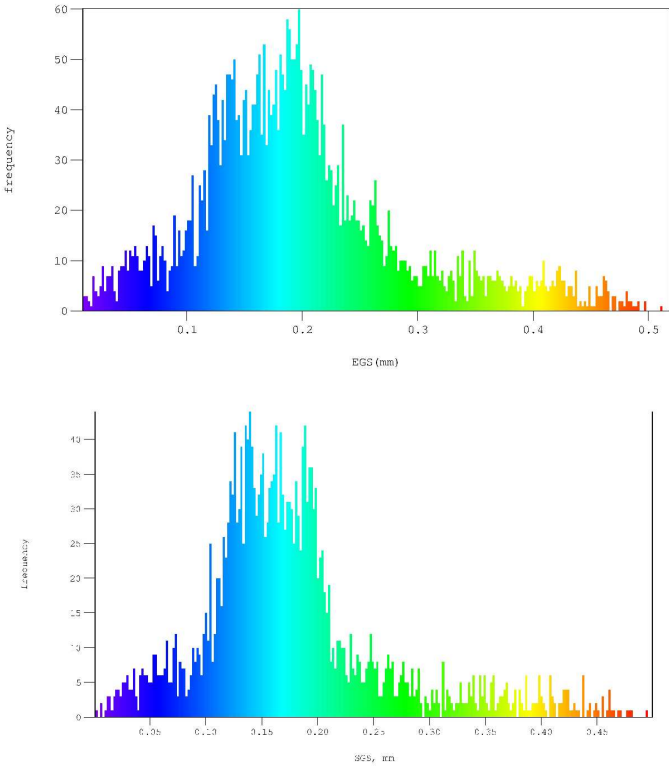


Fig.29b
202x273mm (600 x 600 DPI)

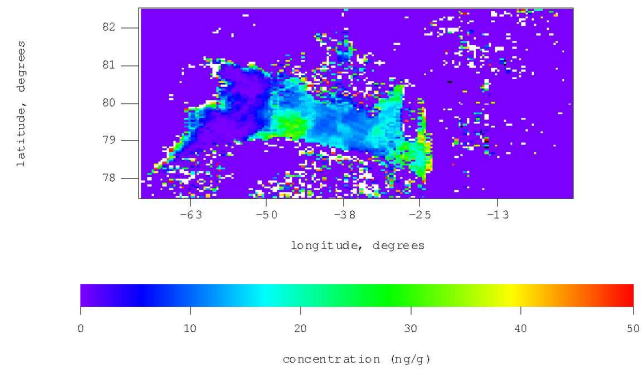


Fig.30
202x273mm (600 x 600 DPI)

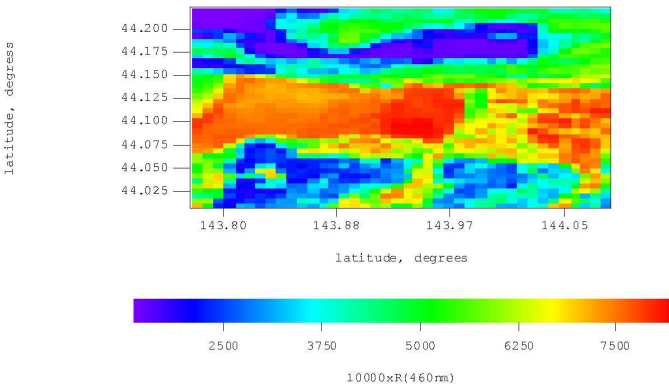


Fig.31a
202x273mm (600 x 600 DPI)

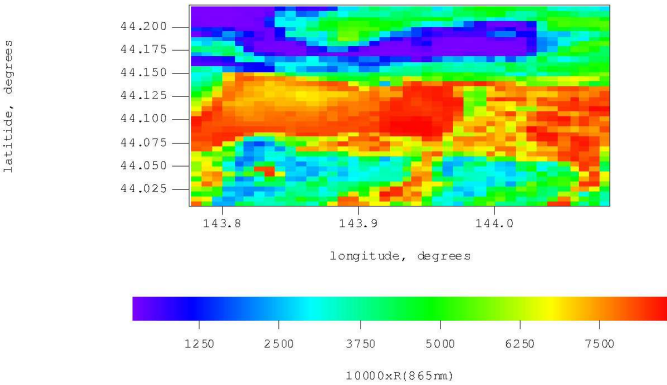


Fig.31b
202x273mm (600 x 600 DPI)

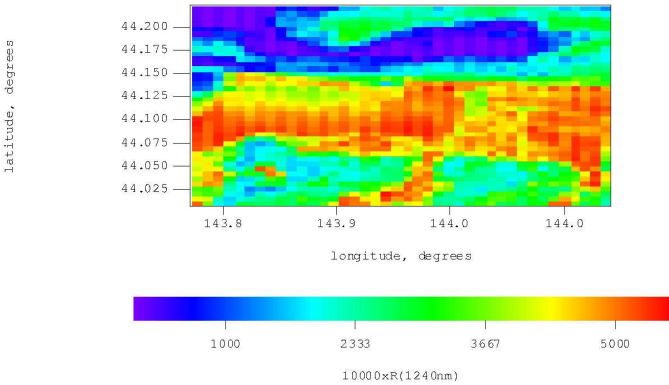


Fig.31c
202x273mm (600 x 600 DPI)

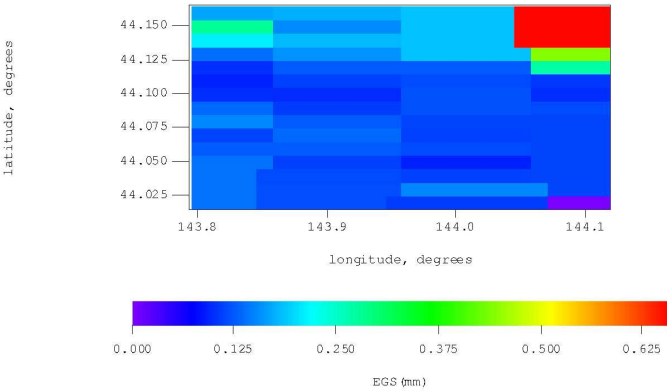


Fig.31d
202x273mm (600 x 600 DPI)

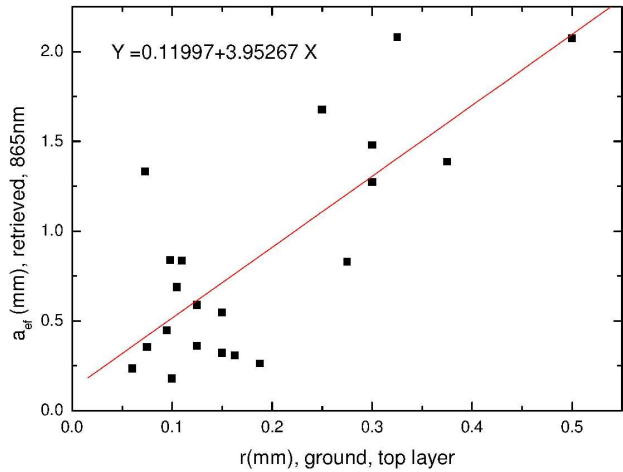


Fig.32a
202x273mm (600 x 600 DPI)

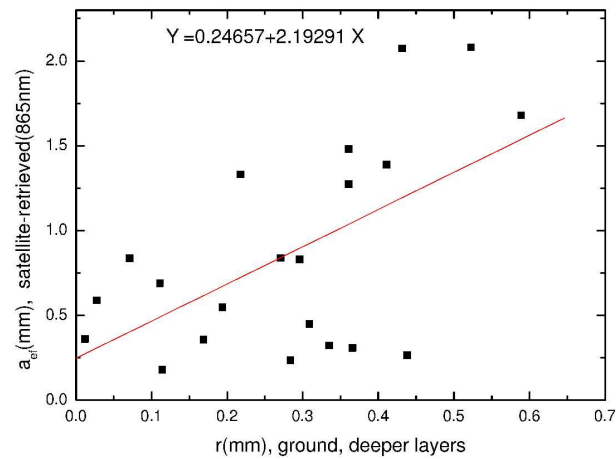


Fig.32b
202x273mm (600 x 600 DPI)

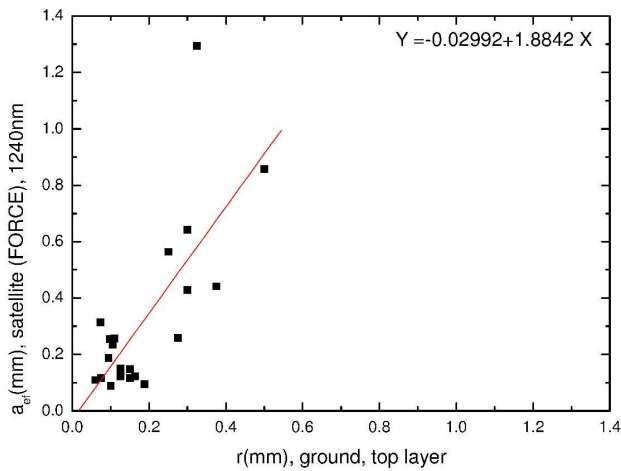


Fig.33
202x273mm (600 x 600 DPI)

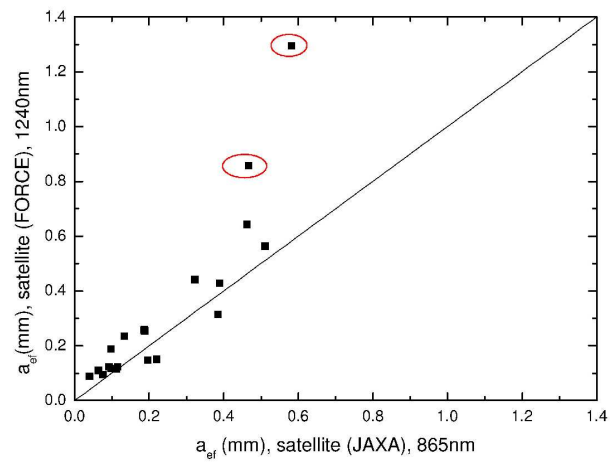


Fig.34
202x273mm (600 x 600 DPI)

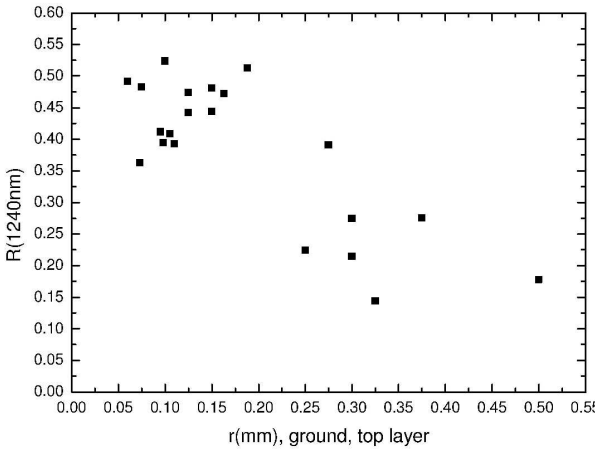


Fig.35
202x273mm (600 x 600 DPI)